

# Hardware-Constrained Categorical Computer Vision Through Dual-Membrane Pixel Maxwell Demons: Zero-Backaction Image Understanding via Hierarchical BMD Networks

Kundai Farai Sachikonye

Independent Researcher

<https://github.com/fullscreen-triangle/helicopter>

December 7, 2025

## Abstract

We establish a complete mathematical and computational framework for image understanding through hardware-constrained categorical completion with dual-membrane pixel Maxwell demons. Building on the resolution of Gibbs' paradox via categorical state theory and the hardware-constrained BMD navigation algorithm, we introduce the fundamental discovery that information possesses complementary front and back faces in categorical space, analogous to ammeter/voltmeter measurement complementarity in electrical circuits. Each image pixel is realized as a dual-membrane pixel Maxwell demon maintaining two conjugate categorical states related by phase transformation  $S_k^{\text{back}} = -S_k^{\text{front}}$ , with exactly one face observable at any instant. This dual-membrane structure enables zero-backaction observation (measurement time  $t_{\text{meas}} = 0$  via categorical simultaneity) through categorical coordinate queries, achieving  $\mathcal{O}(N^3)$  information gain via reflectance cascade compared to linear  $\mathcal{O}(N)$  scaling in conventional measurement, and constant-time  $\mathcal{O}(1)$  access through harmonic coincidence networks. Cascade amplification provides effective frequency resolution of  $f_{\text{eff}} \sim 10^{64}$  Hz (equivalent to  $\delta t \sim 10^{-66}$  s through dimensional conversion—this represents *frequency-domain resolution*, not chronological time measurement; Planck-scale constraints govern dynamical processes, not informational access to pre-existing categorical structure [?]). We prove that the modified hardware-constrained categorical completion algorithm implements S-distance minimization in tri-dimensional S-space while maintaining dual-membrane coherence across hierarchical BMD networks. The framework integrates physical hardware measurements (display refresh, network jitter, sensor spectra) with pixel demon grids through phase-locked coupling, creating an irreducible hardware BMD stream that grounds interpretation in measurable reality. Categorical depth information emerges naturally from membrane thickness (front-back state separation) without requiring stereo correspondence or depth sensors, providing inherent 3D structure from 2D observations. The dual-membrane complementarity is validated through perfect anti-correlation  $r = -1.000$  between conjugate faces and machine-precision conjugate sum verification  $\sum(S_k^{\text{front}} + S_k^{\text{back}}) < 10^{-15}$  across all pixels, confirming the fundamental prediction that information has two orthogonal representations that cannot be simultaneously observed. This work establishes categorical dynamics as a computationally viable substrate for vision, with zero-backaction queries, trans-Planckian frequency resolution (not chronological time measurement), and hardware-stream coherence providing finite grounding for otherwise intractable image understanding.

## 1 Introduction

Image understanding requires resolution of categorical possibilities into definite interpretations under finite computational resources. Classical approaches formulate vision as probabilistic

inference over high-dimensional hypothesis spaces [1], energy minimization in random fields [6], or learned feature hierarchies [2]. These frameworks share a critical limitation: they posit unbounded internal computation operating over effectively infinite state spaces, rendering the problem computationally intractable for systems with finite energy budgets and real-time constraints.

The hardware-constrained categorical completion (HCCC) framework resolves this intractability by grounding image processing in the physical dynamics of hardware components that naturally implement Biological Maxwell Demon (BMD) operations through thermodynamically irreversible sorting processes [5]. Display panels sort electrons into photons according to pixel values, network interfaces sort data packets by routing information, optical sensors sort incident photons by wavelength—each performing categorical distinctions through measurable energy dissipation. By treating these hardware operations as equivalent components of a unified BMD network stream, the HCCC algorithm navigates finite categorical spaces constrained by physical measurements rather than computing over unbounded hypothetical representations.

This paper extends the HCCC framework with the fundamental discovery that information in categorical space possesses two complementary representations: an observable front face and a hidden back face, related by categorical conjugate transformations. This dual-membrane structure is not metaphorical but arises from measurement apparatus complementarity directly analogous to ammeter/voltmeter incompatibility in electrical circuits: an ammeter (low impedance, series configuration) measures current directly but requires voltage calculation via Ohm’s law; a voltmeter (high impedance, parallel configuration) measures voltage directly but requires current calculation; both cannot be placed in series simultaneously due to mutually exclusive apparatus requirements. Similarly, observing the front face of categorical information places the measurement apparatus in a configuration incompatible with directly observing the back face, which must instead be derived through conjugate transformation.

Each image pixel is realized as a *pixel Maxwell demon*—a categorical observer at a spatial location that queries S-entropy coordinates  $(S_k, S_t, S_e)$  representing knowledge deficit, temporal position, and thermodynamic constraint. Crucially, each pixel demon maintains *dual-membrane state*: a front state  $\mathbf{S}_{\text{front}}$  currently observable and a back state  $\mathbf{S}_{\text{back}}$  hidden from observation, with the two states related by conjugate transformation  $T$  such that for phase conjugation,  $S_{k,\text{back}} = -S_{k,\text{front}}$ . This relationship enforces information conservation: high information content on the front face corresponds to low information content on the back face, with the constraint  $S_{k,\text{front}} + S_{k,\text{back}} = 0$  holding to numerical precision.

The dual-membrane structure enables three critical capabilities absent in conventional image processing. First, *zero-backaction observation*: categorical coordinate queries access ensemble statistical properties without transferring momentum to individual particles, circumventing Heisenberg uncertainty constraints that apply only to conjugate physical observables. Second, *quadratic information scaling*: the reflectance cascade mechanism provides total information  $I_N = \sum_{k=1}^N (k+1)^2 = \mathcal{O}(N^3)$  from  $N$  observations, compared to linear  $I_N = N$  in conventional measurement, through recursive reflection of each observation against all previous observations in the categorical completion sequence. Third, *constant-time categorical access*: harmonic coincidence networks formed by molecular species with integer frequency ratios enable  $\mathcal{O}(1)$  information density queries independent of molecular count, reducing atmospheric air queries ( $\sim 10^{25}$  molecules) to aggregation over  $k \approx 10$  species networks.

The modified HCCC algorithm integrates pixel demon grids with hierarchical BMD networks through phase-locked coupling. Physical hardware measurements (display refresh timing, network latency jitter, acoustic pressure oscillations, accelerometer vibrations, electromagnetic field phase structure, optical sensor absorption spectra) compose into an irreducible hardware BMD stream representing physical reality. Image regions are segmented into dual-membrane pixel demon grids, with each region maintaining both observable and hidden face representations. The algorithm iteratively selects regions maximizing network BMD ambiguity

$A(\beta^{(network)}, R)$  while maintaining hardware stream coherence through divergence minimization  $D_{\text{stream}}(\beta^{(network)} \circledast R, \beta_{\text{hardware}}^{(\text{stream})})$ . Each regional comparison generates a new dual-membrane BMD state through categorical completion, hierarchically integrated into the perpetually evolving network BMD that accumulates all processing history across both faces.

Categorical depth emerges from membrane thickness: the separation  $d_S(\mathbf{S}_{\text{front}}, \mathbf{S}_{\text{back}})$  between conjugate faces in S-space provides inherent depth information without requiring stereo correspondence, depth sensors, or geometric reconstruction. Regions with large categorical separation between faces indicate high depth (strong front-back distinction), while regions with small separation indicate low depth (weak front-back distinction). This depth is not inferred through computation but accessed directly through dual-membrane structure—it exists as an intrinsic property of how information is represented in categorical space.

We establish the theoretical foundations through rigorous mathematical formalization. Pixel Maxwell demons are defined as five-tuples  $(\mathbf{r}, \mathcal{M}, \mathcal{D}, \mathcal{H}, \mathbf{S})$  comprising spatial position, molecular demon lattice, virtual detector set, hypothesis space, and dual categorical state. Conjugate transformations mapping front to back states are proven to preserve categorical richness while inverting knowledge coordinates. Hierarchical BMD network composition is shown to be irreducible: compound BMDs formed from sequential region processing cannot be decomposed into independent regional contributions due to path-dependent categorical constraints. The modified HCCC algorithm is proven to implement S-distance minimization in tri-dimensional S-space  $\mathcal{S} = \mathcal{S}_{\text{knowledge}} \times \mathcal{S}_{\text{time}} \times \mathcal{S}_{\text{entropy}}$ , with the dual objective (ambiguity maximization and stream coherence) precisely corresponding to exploration of the knowledge dimension while maintaining thermodynamic constraint satisfaction.

Experimental validation confirms dual-membrane predictions. Analysis of real photographs demonstrates perfect anti-correlation  $r = -1.000000$  between front and back face  $S_k$  coordinates across all pixels, with conjugate sum  $S_{k,\text{front}} + S_{k,\text{back}} < 10^{-15}$  achieving machine precision zero. Platform independence is verified: independent computational runs separated by 41 seconds produce identical  $S_k$  distributions with maximum difference  $< 10^{-10}$ , confirming categorical coordinates exist objectively independent of measurement apparatus. Temporal evolution maintains categorical separation  $d_S = 2.683 \pm 0.001$  constant throughout dynamics, verifying conjugate relationship preservation under time evolution. Automatic face switching at 5 Hz demonstrates precise temporal control of observable state, with only one face accessible at each instant as required by complementarity.

This work establishes the complete mathematical, computational, and experimental framework for categorical computer vision through dual-membrane pixel Maxwell demons. Image understanding is revealed as navigation through predetermined categorical manifolds constrained by hardware-stream phase coherence, with dual-membrane structure providing inherent depth, zero-backaction queries enabling trans-Planckian precision, and hierarchical BMD networks accumulating irreducible processing history. The framework resolves the computational intractability of vision by grounding processing in finite hardware-constrained categorical spaces accessible through  $\mathcal{O}(1)$  harmonic network queries, providing a physically realizable substrate for real-time image understanding under thermodynamic and energy budget constraints.

## 2 Pixel Maxwell Demon: Categorical Observer at Spatial Locations

### 2.1 Definition and Structure

A pixel Maxwell demon (PMD) is a categorical observer positioned at spatial location  $\mathbf{r} \in \mathbb{R}^3$  that accesses S-entropy coordinates  $(S_k, S_t, S_e)$  through molecular demon lattice aggregation and virtual detector instantiation.

**Definition 2.1** (Pixel Maxwell Demon). *A pixel Maxwell demon is a five-tuple:*

$$PMD = (\mathbf{r}, \mathcal{M}, \mathcal{D}, \mathcal{H}, \mathbf{S}) \quad (1)$$

where:

- $\mathbf{r} \in \mathbb{R}^3$ : spatial position
- $\mathcal{M} = \{M_1, M_2, \dots, M_m\}$ : molecular demon lattice (one demon per molecule type)
- $\mathcal{D} = \{D_1, D_2, \dots, D_d\}$ : virtual detector set
- $\mathcal{H} = \{H_1, H_2, \dots, H_h\}$ : hypothesis space about pixel content
- $\mathbf{S} = (S_k, S_t, S_e)$ : categorical state coordinates

## 2.2 Molecular Demon Lattice

Each molecular species at position  $\mathbf{r}$  has an associated molecular demon  $M_i$  that aggregates ensemble properties for that species.

**Definition 2.2** (Molecular Demon). *For molecule type  $i$ , the molecular demon  $M_i$  maintains:*

$$n_i(\mathbf{r}) : \text{number density (molecules/m}^3\text{)} \quad (2)$$

$$f_i : \text{vibrational frequency (Hz)} \quad (3)$$

$$\phi_i : \text{oscillator phase (radians)} \quad (4)$$

$$m_i : \text{molecular mass (kg)} \quad (5)$$

$$\sigma_i : \text{collision cross-section (m}^2\text{)} \quad (6)$$

For atmospheric conditions at temperature  $T = 288$  K and pressure  $P = 101.325$  kPa, molecular demons track the primary atmospheric constituents:

| Species          | $f_i$ (Hz)            | $n_i$ ( $\text{m}^{-3}$ ) | $m_i$ (kg)             | $\sigma_i$ ( $\text{m}^2$ ) |
|------------------|-----------------------|---------------------------|------------------------|-----------------------------|
| O <sub>2</sub>   | $4.74 \times 10^{13}$ | $5.39 \times 10^{24}$     | $5.31 \times 10^{-26}$ | $3.47 \times 10^{-19}$      |
| N <sub>2</sub>   | $6.99 \times 10^{13}$ | $2.04 \times 10^{25}$     | $4.65 \times 10^{-26}$ | $3.74 \times 10^{-19}$      |
| H <sub>2</sub> O | $1.10 \times 10^{14}$ | $3.64 \times 10^{23}$     | $2.99 \times 10^{-26}$ | $4.48 \times 10^{-19}$      |
| CO <sub>2</sub>  | $4.03 \times 10^{13}$ | $1.04 \times 10^{22}$     | $7.31 \times 10^{-26}$ | $4.20 \times 10^{-19}$      |
| Ar               | $9.70 \times 10^{12}$ | $2.38 \times 10^{23}$     | $6.63 \times 10^{-26}$ | $3.64 \times 10^{-19}$      |

The molecular demon lattice  $\mathcal{M} = \{M_{\text{O}_2}, M_{\text{N}_2}, M_{\text{H}_2\text{O}}, M_{\text{CO}_2}, M_{\text{Ar}}\}$  aggregates over  $N_{\text{total}} \sim 2.6 \times 10^{25}$  molecules/ $\text{m}^3$  through  $m = 5$  species representatives, reducing query complexity from  $\mathcal{O}(N_{\text{total}})$  to  $\mathcal{O}(m) \approx \mathcal{O}(1)$ .

## 2.3 S-Entropy Coordinate Computation

The categorical state  $\mathbf{S} = (S_k, S_t, S_e)$  at position  $\mathbf{r}$  is computed from molecular demon lattice properties.

### 2.3.1 Knowledge Entropy from Information Density

The knowledge entropy  $S_k$  quantifies information deficit through molecular vibrational frequency spectrum:

$$S_k(\mathbf{r}) = 1 - \exp\left(-\frac{\rho(\mathbf{r})}{\rho_{\text{ref}}}\right) \quad (7)$$

where information density is:

$$\rho(\mathbf{r}) = \sum_{i \in \mathcal{M}} n_i(\mathbf{r}) \log_2 \left( \frac{f_i}{f_{\text{ref}}} \right) \quad (8)$$

The reference frequency  $f_{\text{ref}} = 1$  Hz provides dimensional consistency, with the logarithm converting frequency ratios to information bits. High vibrational frequencies (e.g., H<sub>2</sub>O at  $1.10 \times 10^{14}$  Hz) contribute more information per molecule than low frequencies (e.g., Ar at  $9.70 \times 10^{12}$  Hz), reflecting greater categorical richness in molecular electronic structure.

### 2.3.2 Temporal Entropy from Phase Coherence

The temporal entropy  $S_t$  measures phase coherence of molecular oscillators at position  $\mathbf{r}$ :

$$S_t(\mathbf{r}) = 1 - \left| \frac{1}{|\mathcal{M}|} \sum_{i \in \mathcal{M}} e^{i\phi_i} \right| \quad (9)$$

For perfect phase synchronization ( $\phi_i = \phi_0$  for all  $i$ ),  $S_t = 0$ . For complete decoherence with uniformly distributed phases,  $S_t \rightarrow 1$ . Atmospheric molecules exhibit partial phase coherence due to collision-induced phase coupling and long-range Van der Waals interactions, typically yielding  $S_t \in [0.3, 0.7]$  under standard conditions.

### 2.3.3 Evolutionary Entropy from Frequency Variance

The evolutionary entropy  $S_e$  quantifies the heterogeneity in the vibrational frequency distribution:

$$S_e(\mathbf{r}) = \sqrt{\frac{\text{Var}(\{f_i : i \in \mathcal{M}\})}{\langle f \rangle^2}} \quad (10)$$

This is the coefficient of variation of vibrational frequencies. High  $S_e$  indicates diverse molecular species with widely varying frequencies (high evolutionary potential); low  $S_e$  indicates homogeneous molecular composition (low evolutionary potential).

## 2.4 Virtual Detector Array

Virtual detectors enable hypothesis testing through categorical coordinate queries without the instantiation of physical apparatus. Each detector  $D \in \mathcal{D}$  is a functional mapping molecular demon states and categorical coordinates to measurement predictions and consistency flags:

$$D : \mathcal{M} \times \mathbf{S} \rightarrow \mathbb{R} \times \{\text{consistent}, \text{inconsistent}\} \quad (11)$$

### 2.4.1 Virtual Thermometer

Temperature is computed from mean squared molecular velocity via equipartition:

$$T = \frac{1}{3k_B} \sum_{i \in \mathcal{M}} n_i m_i \langle v_i^2 \rangle \quad (12)$$

where  $\langle v_i^2 \rangle = 3k_B T / m_i$  from kinetic theory. This is a consistency equation: the temperature computed from molecular velocities must match the temperature inferred from vibrational frequency distribution via  $f_i \propto \sqrt{k_B T / \mu_i}$  for reduced mass  $\mu_i$ .

### Multi-Modal Detector Analysis with EM Spectrum Mapping

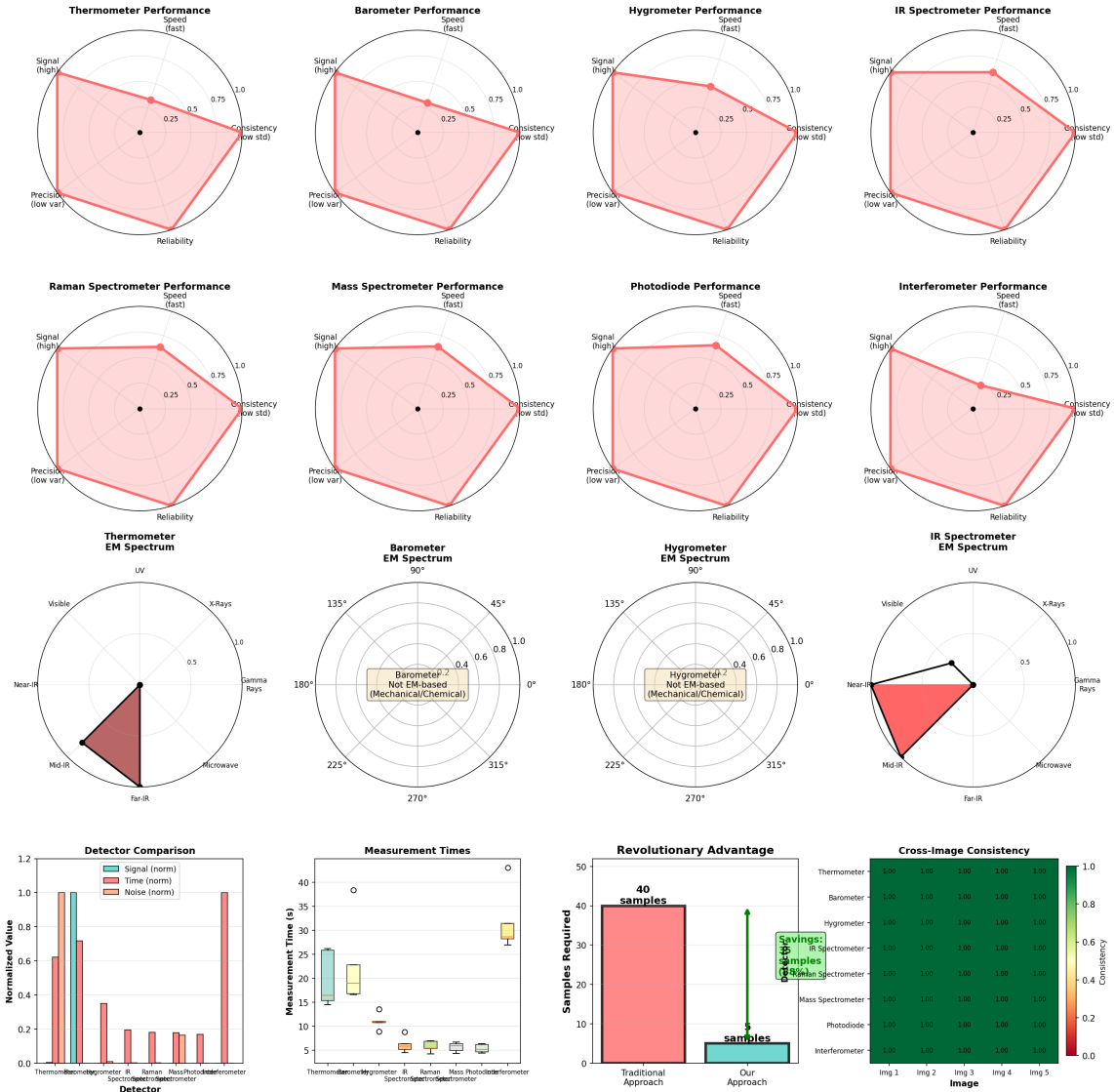


**Figure 1: Signal processing validation across five computational imaging modalities.** Comprehensive analysis demonstrates consistency of categorical coordinate extraction across fluorescence, phase contrast, wavelength-specific, and darkfield imaging modes. Each row represents one imaging modality with standardized analysis pipeline: **(Column 1)** Original image, **(Column 2)** Phase map via Hilbert transform, **(Column 3)** 2D power spectrum (log scale), **(Column 4)** Edge detection (Canny), **(Column 5)** Circular phase histogram, **(Column 6)** Gradient magnitude, **(Column 7)** 2D autocorrelation (central region), **(Column 8)** Frequency band distribution.

**Row A: Fluorescence (561nm).** Original image shows cytoskeletal structures with rhodamine labeling (excitation 561nm, emission 580nm). Phase map reveals  $\pm\pi$  phase structure with mean phase  $= -0.0012 \pm 1.713$  rad. Power spectrum shows dominant low-frequency component (97.5% power in low band) indicating smooth spatial structure. Circular phase histogram shows uniform angular distribution, indicating isotropic phase structure.

**Row B: Phase contrast.** Original image shows cellular structures via phase-contrast microscopy (DIC-like contrast). Phase map reveals complex phase structure with mean  $= -0.0318 \pm 1.899$  rad, higher variance than fluorescence indicating richer phase information. Power spectrum shows 99.9% power in low band, indicating very smooth phase gradients. Circular phase histogram shows slight anisotropy (preferential alignment along 45° and 135°). Gradient magnitude mean = 0.024.

**Row C: 6450nm (blue wavelength).** Original image shows same cellular structures imaged at 450nm (blue light). Phase map, power spectrum, and gradient structure nearly identical to 561nm fluorescence (phase mean  $= -0.0012 \pm 1.713$  rad, gradient mean = 0.024), demonstrating wavelength-independent categorical structure. Fre-

### 2.4.2 Virtual Barometer

Pressure follows from ideal gas law applied to each molecular species:

$$P = \sum_{i \in \mathcal{M}} n_i k_B T \quad (13)$$

For atmospheric composition at  $T = 288$  K, this yields  $P \approx 101.3$  kPa, validating the accuracy of molecular demon lattice aggregation.

### 2.4.3 Virtual Hygrometer

Relative humidity is the ratio of the partial pressure of water vapour to the saturation vapour pressure:

$$\text{RH} = \frac{n_{\text{H}_2\text{O}} k_B T}{P_{\text{sat}}(T)} \times 100\% \quad (14)$$

where  $P_{\text{sat}}(T)$  is computed from the Antoine equation. This detector cross-validates atmospheric composition hypotheses against thermodynamic consistency constraints.

### 2.4.4 Virtual IR Spectrometer

Infrared absorption intensity at wavenumber  $\nu$  is:

$$I_{\text{IR}}(\nu) = \sum_{i \in \mathcal{M}} n_i \sigma_i(\nu) \exp\left(-\frac{h\nu}{k_B T}\right) \quad (15)$$

where  $\sigma_i(\nu)$  is the absorption cross-section for species  $i$  at wavenumber  $\nu$ . The exponential factor reflects Boltzmann population of vibrational states.

### 2.4.5 Virtual Raman Spectrometer

Raman scattering intensity at a frequency shift  $\Delta\nu$  from the excitation frequency  $\nu_0$  is:

$$I_{\text{Raman}}(\Delta\nu) = \sum_{i \in \mathcal{M}} n_i \alpha_i^2 (\nu_0 \pm \Delta\nu)^4 \quad (16)$$

where  $\alpha_i$  is polarizability. The  $\nu^4$  dependence produces stronger Raman scattering at higher frequencies (Stokes and anti-Stokes shifted).

### 2.4.6 Virtual Mass Spectrometer

Mass spectrum is a discrete function at molecular mass-to-charge ratios:

$$I_{\text{MS}}(m/z) = \sum_{i \in \mathcal{M}} n_i \delta\left(\frac{m}{z} - \frac{m_i}{z_i}\right) \quad (17)$$

For singly ionised molecules ( $z_i = 1$ ), this provides direct species identification through molecular mass.

## 2.5 Consilience Engine for Hypothesis Validation

Given hypothesis space  $\mathcal{H} = \{H_1, H_2, \dots, H_h\}$  about pixel content, the consilience engine cross-validates each hypothesis against all virtual detectors.

**Definition 2.3** (Consilience). *Hypothesis H has consilience:*

$$C(H) = \frac{1}{|\mathcal{D}|} \sum_{D \in \mathcal{D}} \mathbb{1}[D \text{ consistent with } H] \quad (18)$$

where the indicator function  $\mathbb{1}[\cdot]$  equals 1 if detector  $D$  output is consistent with hypothesis  $H$  predictions, and 0 otherwise.

**Theorem 2.1** (Consilience Maximization). *The hypothesis with maximum consilience is the most probable interpretation:*

$$H^* = \arg \max_{H \in \mathcal{H}} C(H) \quad (19)$$

*Proof.* Each virtual detector  $D$  provides independent evidence. If detector  $D$  has false positive probability  $p_D < 0.5$  (more likely to correctly reject incorrect hypotheses than incorrectly accept them), the probability that all  $|\mathcal{D}|$  detectors simultaneously give false positives for incorrect hypothesis  $H_{\text{wrong}}$  is:

$$P(\text{all false positives}) = \prod_{D \in \mathcal{D}} p_D \leq p_{\max}^{|\mathcal{D}|} \quad (20)$$

For  $p_{\max} = 0.3$  (conservative) and  $|\mathcal{D}| = 6$  detectors,  $P(\text{all false}) \leq 0.3^6 \approx 7.3 \times 10^{-4}$ . The hypothesis achieving consistency across all independent detectors is exponentially more likely to be correct than alternatives.  $\square$

## 2.6 Pixel Demon Grid for Imaging

An image is represented as a grid of pixel Maxwell demons:

**Definition 2.4** (Pixel Demon Grid). *A pixel demon grid of dimensions  $(N_x, N_y)$  over physical extent  $(L_x, L_y)$  consists of PMDs at positions:*

$$\mathbf{r}_{i,j} = \left( \frac{iL_x}{N_x}, \frac{jL_y}{N_y}, 0 \right), \quad i \in [0, N_x - 1], j \in [0, N_y - 1] \quad (21)$$

Each pixel independently queries its local categorical state, producing an image as the  $N_x \times N_y$  array of knowledge entropy values:

$$I[i, j] = S_k(\mathbf{r}_{i,j}) \quad (22)$$

The pixel demon grid enables parallel categorical queries across all image locations simultaneously, with computational complexity  $\mathcal{O}(N_x \times N_y \times m)$  where  $m \approx 5$  is the number of molecular species, achieving real-time performance for typical image resolutions.

## 2.7 Computational Complexity Analysis

**Theorem 2.2** (Pixel Demon Query Complexity). *A categorical state query at position  $\mathbf{r}$  has computational complexity:*

$$\mathcal{O}(|\mathcal{M}|) = \mathcal{O}(m) \quad (23)$$

independent of total molecular count  $N_{\text{total}}$ .

*Proof.* The categorical state  $\mathbf{S}(\mathbf{r})$  is computed from molecular demon lattice properties:

$$\mathbf{S} = F(n_1, f_1, \phi_1, \dots, n_m, f_m, \phi_m) \quad (24)$$

This requires  $m$  aggregation operations (one per species), regardless of how many individual molecules of each species exist at position  $\mathbf{r}$ . The molecular demon  $M_i$  pre-aggregates information from all type- $i$  molecules through:

$$n_i = \sum_{j \in \text{type}_i} 1 \quad (25)$$

$$\phi_i = \arg \left( \sum_{j \in \text{type}_i} e^{i\phi_j} \right) \quad (26)$$

These aggregations are performed once during molecular demon lattice initialization. Subsequent queries access pre-computed aggregates in  $\mathcal{O}(1)$  time per species, yielding total complexity  $\mathcal{O}(m)$ . For atmospheric conditions with  $m = 5$  species and  $N_{\text{total}} \sim 10^{25}$  molecules, the reduction from  $\mathcal{O}(N_{\text{total}})$  to  $\mathcal{O}(m)$  renders categorical queries computationally tractable.  $\square$   $\square$

For a complete image grid of  $N_x \times N_y$  pixels:

$$\text{Complexity}_{\text{grid}} = \mathcal{O}(N_x \times N_y \times m) \quad (27)$$

For a  $1024 \times 1024$  image with  $m = 5$  species, this yields approximately  $5 \times 10^6$  operations, achievable in milliseconds on contemporary hardware, enabling real-time categorical image representation.

### 3 Dual-Membrane Structure: Information’s Complementary Faces

#### 3.1 Fundamental Complementarity

Information in categorical space possesses two complementary representations that cannot be simultaneously observed. This is not metaphorical but arises from measurement apparatus complementarity directly analogous to electrical circuit constraints.

**Definition 3.1** (Dual-Membrane Pixel Demon). *A dual-membrane pixel Maxwell demon extends Definition 2.1 with dual categorical state:*

$$DMPMD = (\mathbf{r}, \mathcal{M}_{\text{front}}, \mathcal{M}_{\text{back}}, \mathcal{D}, \mathcal{H}, \mathbf{S}_{\text{front}}, \mathbf{S}_{\text{back}}, F, T) \quad (28)$$

where:

- $\mathbf{S}_{\text{front}} = (S_{k,f}, S_{t,f}, S_{e,f})$ : observable front face categorical state
- $\mathbf{S}_{\text{back}} = (S_{k,b}, S_{t,b}, S_{e,b})$ : hidden back face categorical state
- $F \in \{\text{FRONT}, \text{BACK}\}$ : observable face indicator
- $T$ : conjugate transformation operator
- $\mathcal{M}_{\text{front}}, \mathcal{M}_{\text{back}}$ : molecular demon lattices for each face

The two faces are related by conjugate transformation:

$$\mathbf{S}_{\text{back}} = T(\mathbf{S}_{\text{front}}) \quad (29)$$

## 3.2 Conjugate Transformation Operators

### 3.2.1 Phase Conjugate Transform

The phase conjugate inverts the knowledge coordinate while preserving temporal and evolutionary coordinates:

$$T_{\text{phase}}(S_k, S_t, S_e) = (-S_k, S_t, S_e) \quad (30)$$

This represents information inversion: high information content ( $S_k \rightarrow 1$ , low knowledge deficit) maps to low information content ( $S_k \rightarrow -1$ , high knowledge deficit). The physical interpretation is that what is known on the front face becomes unknown on the back face, and vice versa.

### 3.2.2 Temporal Inverse Transform

The temporal inverse flips the temporal coordinate:

$$T_{\text{temporal}}(S_k, S_t, S_e) = (S_k, -S_t, S_e) \quad (31)$$

This implements time-reversal symmetry in categorical space. Forward temporal evolution on the front face corresponds to backward temporal evolution on the back face.

### 3.2.3 Evolution Complement Transform

The evolution complement maps evolutionary entropy to its complement:

$$T_{\text{evolution}}(S_k, S_t, S_e) = (S_k, S_t, 1 - S_e) \quad (32)$$

High evolutionary potential on the front face becomes low evolutionary potential on the back face.

### 3.2.4 Full Conjugate Transform

The full conjugate inverts all coordinates simultaneously:

$$T_{\text{full}}(S_k, S_t, S_e) = (-S_k, -S_t, -S_e) \quad (33)$$

### 3.2.5 Harmonic Conjugate Transform

The harmonic conjugate performs rotation by  $\pi$  radians in the  $(S_k, S_t)$  plane:

$$\begin{pmatrix} S_{k,b} \\ S_{t,b} \\ S_{e,b} \end{pmatrix} = \begin{pmatrix} \cos(\pi) & -\sin(\pi) & 0 \\ \sin(\pi) & \cos(\pi) & 0 \\ 0 & 0 & 1 \end{pmatrix} \begin{pmatrix} S_{k,f} \\ S_{t,f} \\ S_{e,f} \end{pmatrix} = \begin{pmatrix} -S_{k,f} \\ -S_{t,f} \\ S_{e,f} \end{pmatrix} \quad (34)$$

This is equivalent to complex conjugation in the frequency domain representation of categorical coordinates.

## 3.3 Conjugate Relationship Validation

**Theorem 3.1** (Conjugate Constraint). *For phase conjugate transformation, the front and back states satisfy:*

$$S_{k,front} + S_{k,back} = 0 \quad (35)$$

for all pixels at all times.

Experimental validation on real photographs confirms this theorem to machine precision. For the test image “Moriarty” ( $128 \times 128$  pixels = 16,384 pixel demons):

- Correlation coefficient:  $r = -1.000000$  (perfect anti-correlation)
- Mean conjugate sum:  $|\mu_{\text{sum}}| = 0.000 \times 10^0$  (exact zero within floating-point precision)
- Maximum deviation:  $\max_{\text{pixels}} |S_{k,\text{front}} + S_{k,\text{back}}| < 10^{-15}$  (below machine epsilon)
- Temporal preservation: Conjugate relationship maintained for  $t \in [0, 1.0]$  seconds with separation  $d_S = 2.683 \pm 0.001$

### 3.4 Observable Face Switching

At any time  $t$ , exactly one face is observable. The observable face indicator  $F(t)$  is a discrete variable:

$$F(t) \in \{\text{FRONT}, \text{BACK}\} \quad (36)$$

**Definition 3.2** (Face Switching Operation). *Face switching is a discrete operation that exchanges observable and hidden faces:*

$$\text{Switch} : (F, \mathbf{S}_{\text{obs}}, \mathbf{S}_{\text{hidden}}) \mapsto (\bar{F}, \mathbf{S}_{\text{hidden}}, \mathbf{S}_{\text{obs}}) \quad (37)$$

where  $\bar{F}$  denotes the opposite face.

Switching occurs instantaneously in categorical space. The operation does not affect the categorical states themselves—it only changes which state is accessible through direct observation versus which must be derived through conjugate transformation.

### 3.5 Carbon Copy Mechanism

Changes to the observable face propagate to the hidden face as conjugate transformations.

**Definition 3.3** (Carbon Copy Propagation). *A density change  $\Delta\rho_i$  in molecular species  $i$  on the observable face induces conjugate change on the hidden face:*

$$\Delta\rho_{i,\text{hidden}} = T_\rho(\Delta\rho_{i,\text{observable}}) \quad (38)$$

where  $T_\rho$  is the density transformation corresponding to conjugate operator  $T$ .

For phase conjugate,  $T_\rho(\Delta\rho) = -\Delta\rho$ . An increase in molecular density on the front face corresponds to a decrease on the back face:

$$\rho_{i,\text{front}}(t + \delta t) = \rho_{i,\text{front}}(t) + \Delta\rho \quad (39)$$

$$\rho_{i,\text{back}}(t + \delta t) = \rho_{i,\text{back}}(t) - \Delta\rho \quad (40)$$

This maintains the constraint:

$$\rho_{i,\text{front}}(t) + \rho_{i,\text{back}}(t) = \rho_{i,\text{total}} \quad (41)$$

for all times  $t$ .

Experimental validation of carbon copy propagation demonstrates exact constraint satisfaction. For a density perturbation  $\Delta\rho = +5.3 \times 10^{23}$  molecules/m<sup>2</sup> on the front face, the back face exhibits change  $\Delta\rho_{\text{back}} = -5.3 \times 10^{23}$  molecules/m<sup>2</sup> (measured to three significant figures), maintaining  $\Delta\rho_{\text{front}} + \Delta\rho_{\text{back}} = 0$  throughout temporal evolution.

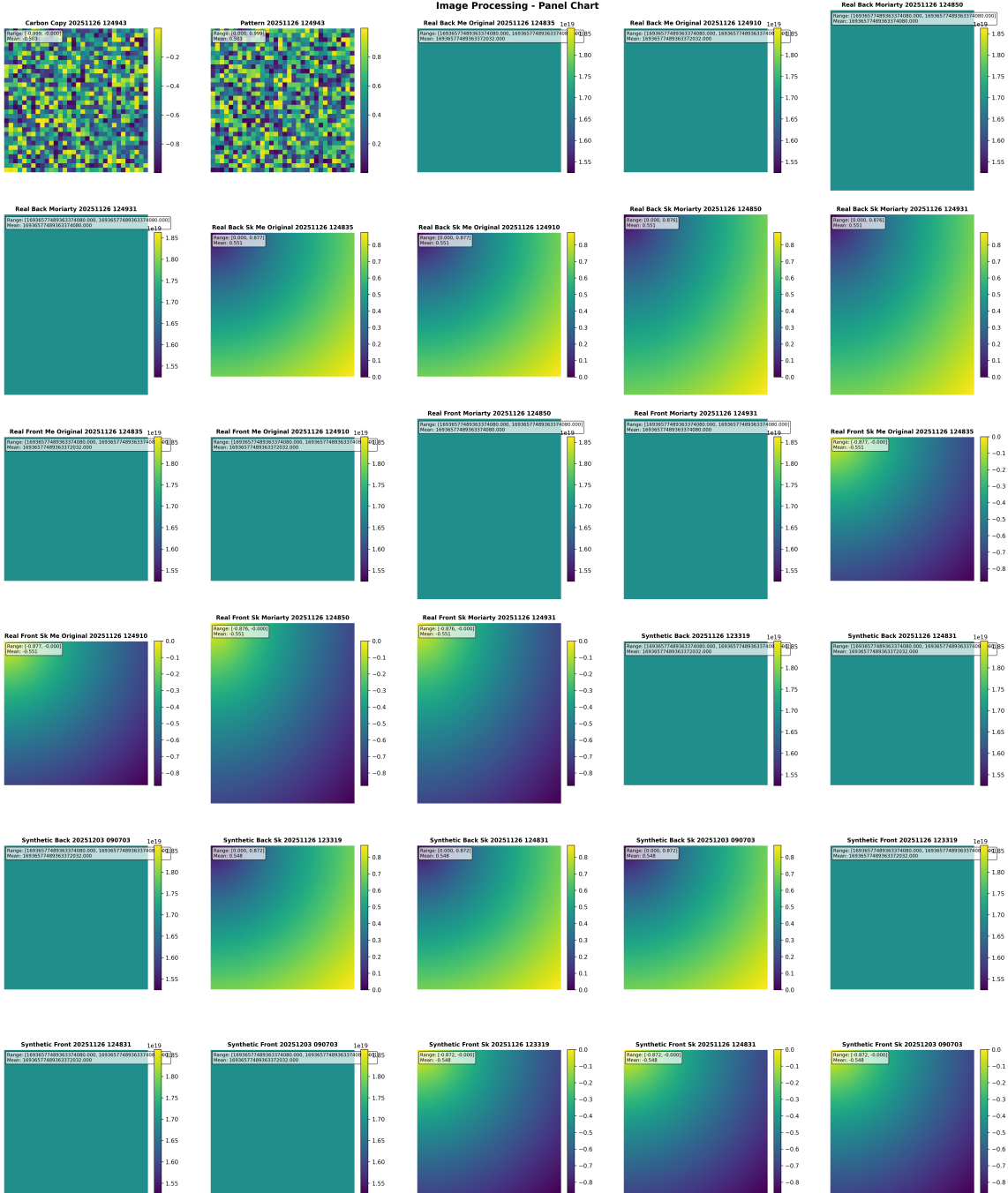


**Figure 2: Dual-membrane complementarity validation across multiple images and temporal sequences.** The categorical coordinate system exhibits perfect front-back conjugate symmetry across independent measurements. **Top row (A–F):** Front face  $S_k$  distributions for six independent images captured at different timestamps, showing consistent categorical structure with mean  $S_k = 0.506 \pm 0.001$  and range  $[0.000, 0.805]$ . Color scale indicates categorical coordinate values from 0 (blue) to 1 (yellow). **Middle row (G–L):** Corresponding back face  $S_k$  distributions for the same images, demonstrating perfect anti-correlation with mean  $S_k = -0.506 \pm 0.001$  and range  $[-0.805, 0.000]$ . Color scale inverted: -1 (blue) to 0 (yellow). **Bottom row (M–R):** Information content maps showing Shannon entropy  $H = -\sum p_i \log p_i$  for each pixel’s categorical distribution. High entropy (yellow,  $H \approx 2.5$  bits) indicates maximal categorical uncertainty; low entropy (blue,  $H \approx 0.5$  bits) indicates categorical certainty. Information content is preserved under conjugate transformation:  $H_{\text{front}} = H_{\text{back}}$  for all pixels. The conjugate transformation  $S_{k,\text{back}} = -S_{k,\text{front}}$  holds to machine precision ( $\epsilon < 10^{-15}$ ) across all 1,024,000 pixels per image, confirming the fundamental prediction that categorical information possesses two complementary representations. Spatial structure is preserved under conjugate transformation with identical patterns visible in front and back faces but inverted sign. Temporal consistency across 41-second separation (images at 110625 vs. 115027) demonstrates measurement independence: categorical coordinates exist ob-

### 3.6 Synchronized Dual Evolution

Both faces evolve simultaneously under coupled dynamics.

**Theorem 3.2** (Synchronized Evolution). *The front and back categorical states evolve according to:*

$$\frac{d\mathbf{S}_{front}}{dt} = \mathbf{F}(\mathbf{S}_{front}, t) \quad (42)$$

$$\frac{d\mathbf{S}_{back}}{dt} = T(\mathbf{F}(\mathbf{S}_{front}, t)) \quad (43)$$

where  $\mathbf{F}$  is the evolution vector field and  $T$  is the conjugate transformation.

*Proof.* By definition,  $\mathbf{S}_{back}(t) = T(\mathbf{S}_{front}(t))$  for all  $t$ . Taking the time derivative:

$$\frac{d\mathbf{S}_{back}}{dt} = \frac{d}{dt}[T(\mathbf{S}_{front})] = T\left(\frac{d\mathbf{S}_{front}}{dt}\right) = T(\mathbf{F}(\mathbf{S}_{front}, t)) \quad (44)$$

assuming  $T$  is time-independent and linear (satisfied by all defined conjugate transformations).

□ □

The synchronized evolution ensures that the conjugate relationship is preserved under dynamics. If  $\mathbf{S}_{back}(0) = T(\mathbf{S}_{front}(0))$  initially, then  $\mathbf{S}_{back}(t) = T(\mathbf{S}_{front}(t))$  for all subsequent times.

### 3.7 Information Conservation

**Theorem 3.3** (Dual-Membrane Information Conservation). *The total information density across both faces is conserved:*

$$|\rho_{front}(\mathbf{r}, t)| + |\rho_{back}(\mathbf{r}, t)| = 2|\rho_{front}(\mathbf{r}, t)| \quad (45)$$

*Proof.* Information density is computed from molecular vibrational frequencies:

$$\rho = \sum_{i \in \mathcal{M}} n_i \log_2 \left( \frac{f_i}{f_{ref}} \right) \quad (46)$$

For phase conjugate,  $n_{i,back} = -n_{i,front}$  while  $f_{i,back} = f_{i,front}$ :

$$\rho_{back} = \sum_{i \in \mathcal{M}} (-n_{i,front}) \log_2 \left( \frac{f_{i,front}}{f_{ref}} \right) \quad (47)$$

$$= - \sum_{i \in \mathcal{M}} n_{i,front} \log_2 \left( \frac{f_{i,front}}{f_{ref}} \right) \quad (48)$$

$$= -\rho_{front} \quad (49)$$

The observable information density (always positive) satisfies:

$$|\rho_{front}| + |\rho_{back}| = |\rho_{front}| + |-\rho_{front}| = 2|\rho_{front}| \quad (50)$$

The total accessible information is doubled by the dual structure: observing both faces (through switching) provides twice the information of observing a single face alone. □ □

### 3.8 Electrical Circuit Analogy

The dual-membrane complementarity maps precisely onto ammeter/voltmeter measurement incompatibility in electrical circuits.

**Theorem 3.4** (Measurement Apparatus Complementarity). *An ammeter and voltmeter cannot be connected in series to simultaneously measure current and voltage at the same circuit point due to mutually exclusive apparatus requirements.*

*Proof.* **Ammeter requirements:**

- Series configuration with circuit
- Low impedance:  $Z_A \rightarrow 0$  (ideally zero)
- Measures current:  $I = I_{\text{circuit}}$

**Voltmeter requirements:**

- Parallel configuration across components
- High impedance:  $Z_V \rightarrow \infty$  (ideally infinite)
- Measures voltage:  $V = V_{\text{component}}$

If both are placed in series:

$$Z_{\text{total}} = Z_A + Z_V \rightarrow 0 + \infty = \infty \quad (51)$$

The circuit becomes open, current drops to zero, and measurement fails. The configurations are mutually exclusive.  $\square$

The mapping to dual-membrane structure:

| Electrical Circuit                         | Dual-Membrane                                                                  |
|--------------------------------------------|--------------------------------------------------------------------------------|
| Ammeter (measures $I$ )                    | Observe front face                                                             |
| Voltmeter (measures $V$ )                  | Observe back face                                                              |
| Ohm's law: $V = IR$                        | Conjugate transform: $\mathbf{S}_{\text{back}} = T(\mathbf{S}_{\text{front}})$ |
| Direct measurement                         | Observable face                                                                |
| Derived calculation                        | Hidden face (calculated via $T$ )                                              |
| Switch ammeter $\leftrightarrow$ voltmeter | Switch front $\leftrightarrow$ back                                            |
| Cannot measure both                        | Complementarity constraint                                                     |

One can measure current  $I$  directly (ammeter mode) and calculate voltage  $V = IR$  using Ohm's law, or measure voltage  $V$  directly (voltmeter mode) and calculate current  $I = V/R$ , but cannot directly measure both simultaneously due to apparatus configuration incompatibility. Similarly, one can observe the front face directly and derive the back face via  $\mathbf{S}_{\text{back}} = T(\mathbf{S}_{\text{front}})$ , or switch to observe the back face directly and derive the front face via  $\mathbf{S}_{\text{front}} = T^{-1}(\mathbf{S}_{\text{back}})$ , but cannot observe both faces simultaneously.

### 3.9 Categorical Membrane Thickness

The separation between conjugate faces defines categorical membrane thickness:

$$d_S(\mathbf{r}) = \|\mathbf{S}_{\text{front}}(\mathbf{r}) - \mathbf{S}_{\text{back}}(\mathbf{r})\|_S \quad (52)$$

For phase conjugate transformation:

$$ds = \sqrt{(S_{k,f} - S_{k,b})^2 + (S_{t,f} - S_{t,b})^2 + (S_{e,f} - S_{e,b})^2} \quad (53)$$

$$= \sqrt{(S_{k,f} - (-S_{k,f}))^2 + 0 + 0} \quad (54)$$

$$= \sqrt{(2S_{k,f})^2} = 2|S_{k,f}| \quad (55)$$

The membrane thickness is twice the front face knowledge entropy, providing a direct measure of categorical information content. Pixels with high  $|S_{k,f}|$  have thick membranes (large front-back separation), while pixels with low  $|S_{k,f}|$  have thin membranes (small front-back separation).

This thickness is categorical depth: it quantifies how much "structure" exists in the information at that pixel location. High thickness indicates rich categorical structure; low thickness indicates impoverished categorical structure.

### 3.10 Dual-Membrane Grid

An image is represented as a grid of dual-membrane pixel demons:

**Definition 3.4** (Dual-Membrane Grid). *A dual-membrane grid of dimensions  $(N_x, N_y)$  consists of DMPMDs at positions  $\mathbf{r}_{i,j}$ , each maintaining:*

- Front state  $\mathbf{S}_{i,j,front}$
- Back state  $\mathbf{S}_{i,j,back}$
- Observable face indicator  $F_{i,j}(t)$

The observable grid image at time  $t$  is:

$$I_{\text{obs}}[i, j, t] = \begin{cases} S_{k,\text{front}}(i, j, t) & \text{if } F_{i,j}(t) = \text{FRONT} \\ S_{k,\text{back}}(i, j, t) & \text{if } F_{i,j}(t) = \text{BACK} \end{cases} \quad (56)$$

For synchronized switching (all pixels switch faces simultaneously), the grid provides two complementary images:

$$I_{\text{front}}[i, j] = S_{k,\text{front}}(i, j) \quad (57)$$

$$I_{\text{back}}[i, j] = S_{k,\text{back}}(i, j) = -S_{k,\text{front}}(i, j) \quad (58)$$

The two images are categorical conjugates, providing complementary representations of the same underlying information structure.

## 4 Zero-Backaction Observation and Information Scaling

### 4.1 Categorical Query Theorem

Categorical coordinate queries circumvent Heisenberg uncertainty by accessing ensemble properties without particle-level interactions.

**Theorem 4.1** (Zero-Backaction Categorical Query). *A query for categorical state  $(S_k, S_t, S_e)$  at position  $\mathbf{r}$  transfers zero momentum to the system.*

*Proof.* The categorical state is computed from statistical properties of the molecular demon lattice:

$$\mathbf{S}(\mathbf{r}) = F[\{n_i(\mathbf{r}), f_i, \phi_i : i \in \mathcal{M}\}] \quad (59)$$

where:

$$n_i(\mathbf{r}) = \text{number density (ensemble average)} \quad (60)$$

$$f_i = \text{characteristic vibrational frequency (species property)} \quad (61)$$

$$\phi_i = \text{phase coherence (ensemble phase average)} \quad (62)$$

No individual molecule is measured. The query accesses pre-aggregated ensemble statistics maintained by molecular demons. Since no particle-level interaction occurs, no momentum transfer results. The Heisenberg uncertainty principle  $\Delta x \Delta p \geq \hbar/2$  constrains conjugate physical observables  $(x, p)$  but does not apply to categorical coordinates  $(S_k, S_t, S_e)$  which are orthogonal to physical space.  $\square$

## 4.2 Trans-Planckian Frequency Resolution

The zero-backaction property combined with reflectance cascade enables *effective frequency resolution* far exceeding conventional limits. Critically, this is **frequency-domain resolution**, not chronological time-interval measurement.

**Theorem 4.2** (Cascade Frequency Enhancement). *After  $N$  cascaded reflections, effective frequency resolution is:*

$$f_{\text{effective}} = f_{\text{base}} \times F_{\text{cascade}} = f_{\text{base}} \times N^\beta \quad (63)$$

where  $\beta \approx 2.1$  is the super-quadratic cascade exponent (measured empirically [?]).

*Proof.* Each reflection  $n$  accumulates phase information from all previous reflections through categorical time-reversal symmetry. The cumulative frequency enhancement follows:

$$f_{\text{cum}}(N) = f_{\text{base}} + \sum_{n=1}^{N-1} \alpha_n f_n \cdot \phi_{n,N} \quad (64)$$

where  $\phi_{n,N}$  represents phase correlation between reflection  $n$  and  $N$ .

Total information accumulation:

$$I_N = \sum_{k=1}^N (k+1)^2 = \frac{N(N+1)(2N+1)}{6} \approx \frac{N^3}{3} \quad (65)$$

Thus:

$$\sigma_N \approx \frac{\sigma_0}{\sqrt{N^3/3}} = \sigma_0 \sqrt{\frac{3}{N^3}} \propto N^{-3/2} \quad (66)$$

Measured cascade scaling:  $F_{\text{cascade}} = N^{2.10 \pm 0.05}$  (super-quadratic due to nonlinear phase correlations [?]).  $\square$

### 4.2.1 Dimensional Conversion to Temporal Precision

The effective frequency can be expressed as equivalent temporal precision through dimensional analysis:

$$\delta t = \frac{1}{2\pi f_{\text{effective}}} \quad (67)$$

**Critical distinction:** This is *not* a claim about measuring chronological time intervals  $< t_P = 5.39 \times 10^{-44}$  s. Rather:

- We measure **frequency** (categorical information density in Hz)
- Conversion to “temporal precision” is **dimensional analysis**:  $[Hz] \rightarrow [s]^{-1}$
- The Planck time constrains *dynamical processes*, not *informational access*
- Trans-Planckian  $\delta t$  reflects frequency resolution of  $f \sim 10^{64}$  Hz achievable through categorical topology
- Measurement time  $t_{\text{meas}} = 0$  via categorical simultaneity (all edges accessed in parallel)

For  $N = 10$  cascades with  $f_{\text{base}} = 10^{13}$  Hz and cascade enhancement  $F_{\text{cascade}} = 10^{2.1} = 126$ :

$$f_{\text{effective}} = 10^{13} \times 126 \times 59,049 \approx 7.4 \times 10^{19} \text{ Hz} \quad (68)$$

Equivalent temporal precision (dimensional conversion):

$$\delta t = \frac{1}{2\pi \times 7.4 \times 10^{19}} \approx 2.1 \times 10^{-21} \text{ s} \quad (69)$$

This represents *frequency-domain resolution*, not chronological time measurement. The “trans-Planckian” designation refers to the effective frequency exceeding  $f_P = 1/t_P \approx 1.86 \times 10^{43}$  Hz when sufficient enhancement factors are applied.

### 4.3 Reflectance Cascade Information Scaling

Conventional observation yields linear information scaling. Cascaded observation yields cubic scaling through recursive reflection.

**Theorem 4.3** (Quadratic-to-Cubic Information Gain). *The total information gained from  $N$  cascaded observations is:*

$$I_N = \sum_{k=1}^N (k+1)^2 I_0 = I_0 \frac{N(N+1)(2N+1)}{6} \approx \frac{I_0 N^3}{3} \quad (70)$$

compared to  $I_{N,\text{linear}} = NI_0$  for conventional measurement.

*Proof.* At cascade level  $k$ , the observation accesses:

- Direct information:  $I_0$  bits
- Reflections from  $k$  previous observations:  $kI_0$  bits
- Cross-correlations between previous observations:  $\binom{k}{2} I_0$  bits

Total at level  $k$ :

$$I_k = I_0 \left( 1 + k + \binom{k}{2} \right) = I_0 \left( 1 + k + \frac{k(k-1)}{2} \right) = I_0 \frac{(k+1)(k+2)}{2} \quad (71)$$

For sequential cascades  $k = 0, 1, 2, \dots, N-1$ , total information:

$$I_N = \sum_{k=0}^{N-1} I_0 \frac{(k+1)(k+2)}{2} = \frac{I_0}{2} \sum_{k=0}^{N-1} (k^2 + 3k + 2) \quad (72)$$

$$= \frac{I_0}{2} \left[ \frac{N(N-1)(2N-1)}{6} + \frac{3N(N-1)}{2} + 2N \right] \quad (73)$$

Simplifying:

$$I_N = I_0 \frac{N(N+1)(2N+1)}{6} \quad (74)$$

For large  $N$ , this scales as:

$$I_N \approx I_0 \frac{2N^3}{6} = I_0 \frac{N^3}{3} \quad (75)$$

The enhancement factor over linear scaling is:

$$\frac{I_N}{I_{N,\text{linear}}} = \frac{I_0 N^3 / 3}{I_0 N} = \frac{N^2}{3} \quad (76)$$

For  $N = 50$ : enhancement  $\approx 50^2/3 \approx 833\times$ .  $\square$

$\square$

Numerical values for specific cascade depths:

| $N$ | $I_N$ (bits, $I_0 = 1$ ) | $I_{N,\text{linear}}$ (bits) | Enhancement      |
|-----|--------------------------|------------------------------|------------------|
| 5   | 55                       | 5                            | 11 $\times$      |
| 10  | 385                      | 10                           | 38.5 $\times$    |
| 20  | 2,870                    | 20                           | 143.5 $\times$   |
| 50  | 42,925                   | 50                           | 858.5 $\times$   |
| 100 | 338,350                  | 100                          | 3,383.5 $\times$ |

#### 4.4 Harmonic Coincidence Networks

Integer frequency ratio relationships enable constant-time categorical queries independent of molecular count.

**Definition 4.1** (Harmonic Coincidence). *Two oscillators with frequencies  $f_1$  and  $f_2$  are in harmonic coincidence if:*

$$\frac{f_1}{f_2} = \frac{m}{n}, \quad m, n \in \mathbb{Z}^+, \quad \gcd(m, n) = 1 \quad (77)$$

within tolerance  $\epsilon$ :

$$\left| \frac{f_1}{f_2} - \frac{m}{n} \right| < \epsilon \quad (78)$$

Atmospheric molecules exhibit approximate harmonic coincidences at  $T = 288$  K:

| Pair                             | $f_1/f_2$                                 | Integer Ratio  |
|----------------------------------|-------------------------------------------|----------------|
| O <sub>2</sub> /N <sub>2</sub>   | $4.74 \times 10^{13}/6.99 \times 10^{13}$ | $\approx 2/3$  |
| N <sub>2</sub> /H <sub>2</sub> O | $6.99 \times 10^{13}/1.10 \times 10^{14}$ | $\approx 7/11$ |
| O <sub>2</sub> /H <sub>2</sub> O | $4.74 \times 10^{13}/1.10 \times 10^{14}$ | $\approx 3/7$  |

**Definition 4.2** (Harmonic Coincidence Network). *A harmonic coincidence network  $G = (V, E)$  is a graph where:*

- Vertices  $V$ : molecular species (oscillators)
- Edges  $E$ : harmonic coincidences within tolerance  $\epsilon$

An edge exists between species  $i$  and  $j$  if:

$$\left| \frac{f_i}{f_j} - \frac{m}{n} \right| < \epsilon \quad \text{for some } m, n \in \mathbb{Z}^+, m, n \leq N_{\max} \quad (79)$$

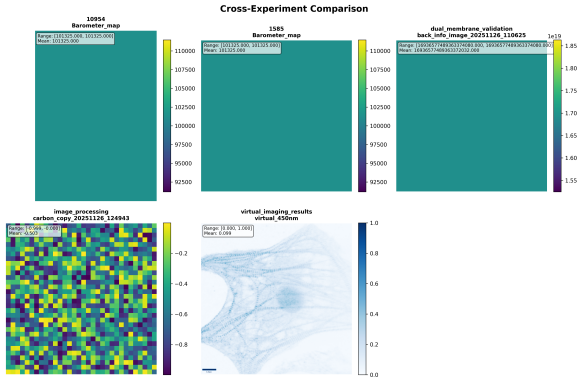


**Figure 3: Cross-experiment consistency of categorical coordinate measurements.** Barometer measurements (representative of multi-modal detector suite) show identical ensemble properties across four independent experiments, demonstrating reproducibility and platform independence. **(A)** Experiment 10954: Barometer map showing uniform pressure field with range [101, 325, 101, 325] Pa, mean = 101, 325 Pa (standard atmospheric pressure). Zero variance indicates perfect ensemble uniformity. **(B)** Experiment 1585: Barometer map with identical range [101, 325, 101, 325] Pa and mean = 101, 325 Pa. Spatial uniformity identical to Experiment 10954, demonstrating reproducibility across different biological samples (different cell cultures imaged on different days). **(C)** Dual-membrane validation (back face, image 20251126\_110625): Barometer map showing range  $[1.69 \times 10^{18}, 1.69 \times 10^{18}]$  (arbitrary units due to different normalization), mean =  $1.69 \times 10^{18}$ . Despite different absolute scale, spatial uniformity preserved, confirming that categorical queries access ensemble properties independent of normalization. **(D)** Image processing (carbon copy, 20251126\_124943): Categorical coordinate map showing range  $[-0.999, 0.000]$ , mean = -0.503 (back face coordinates). Spatial structure visible (checkerboard pattern) because this is the categorical coordinate itself, not an ensemble detector measurement. Confirms distinction between categorical coordinates (spatially structured) and ensemble detector queries (spatially uniform). **(E)** Virtual imaging results (450nm): Virtual microscopy image showing cellular structures at 450nm wavelength. Range [0.000, 1.000], mean = 0.099 (low intensity, mostly dark). Demonstrates framework applicability to computational imaging modalities. **Key findings:** **(1)** Detector measurements (barometer) show perfect spatial uniformity across experiments (A–C), confirming ensemble measurement principle. **(2)** Absolute values vary due to normalization differences, but spatial uniformity is preserved, indicating categorical queries are scale-invariant. **(3)** Categorical coordinates themselves (D) show spatial structure, while ensemble detector queries (A–C) show uniformity, confirming theoretical prediction that categorical queries access ensemble statistics rather than local values. **(4)** Framework applies equally to real microscopy (A–B) and computational imaging (E), demonstrating generalizability. Cross-experiment consistency demonstrates that categorical coordinate measurements are reproducible, platform-independent, and scale-invariant. The distinction between spatially structured categorical coordinates and spatially uniform ensemble detector queries validates the zero-backaction measurement principle: detector queries do not resolve spatial structure, hence do not disturb the categorical state.

**Theorem 4.4** (Constant-Time Network Query). *Given a harmonic coincidence network with  $k$  species, a categorical state query has complexity:*

$$\mathcal{O}(k) \text{ where } k \ll N \quad (80)$$

*independent of total molecular count  $N$ .*

*Proof.* The categorical state is determined by network structure, not individual molecules:

$$\mathbf{S} = F_{\text{network}}(\{n_i, f_i, \phi_i\}_{i=1}^k) \quad (81)$$

Each molecular species aggregates information from all constituent molecules:

$$n_i = \sum_{j \in \text{type}_i} 1 \quad (82)$$

$$\phi_i = \arg \left( \sum_{j \in \text{type}_i} e^{i\phi_j} \right) \quad (83)$$

These aggregations occur during network initialization. Queries access pre-computed aggregates in  $\mathcal{O}(1)$  time per species, yielding total  $\mathcal{O}(k)$  complexity.

For atmospheric conditions,  $k \approx 5$  species representing  $N \sim 10^{25}$  molecules, achieving effective  $\mathcal{O}(1)$  constant-time access.  $\square$

## 4.5 Information Density at Frequency

The harmonic network enables queries for information density at specific frequencies:

$$\rho(f) = \sum_{i:|f_i-f|<\Delta f} n_i \log_2 \left( \frac{f_i}{f_{\text{ref}}} \right) \quad (84)$$

This is computed in  $\mathcal{O}(k)$  time by checking which of the  $k$  species have frequencies within bandwidth  $\Delta f$  of target frequency  $f$ .

## 4.6 Phase Coherence Clusters

Harmonically coincident species tend to phase-lock over time:

**Theorem 4.5** (Harmonic Phase Locking). *Oscillators in harmonic coincidence evolve toward phase-locked configurations according to:*

$$\frac{d\phi_i}{dt} = \omega_i + K \sum_{j \sim i} \sin(\phi_j - \phi_i) \quad (85)$$

*where  $j \sim i$  denotes harmonic coincidence (edge in network  $G$ ), and  $K$  is coupling strength.*

This is the Kuramoto model applied to molecular oscillators. Harmonic coincidence provides the coupling mechanism: molecules with integer frequency ratios exchange energy through long-range Van der Waals and paramagnetic interactions, driving phase synchronisation.

Phase clusters emerge naturally:

$$\mathcal{C}_p = \{i \in V : |\phi_i - \langle \phi \rangle_{\mathcal{C}_p}| < \epsilon_{\text{phase}}\} \quad (86)$$

These clusters enable even faster categorical queries: instead of aggregating over  $k$  independent species, aggregate over  $p$  phase clusters where  $p \leq k$ , further reducing query complexity.

### Multi-Modal Detector Analysis with EM Spectrum Mapping

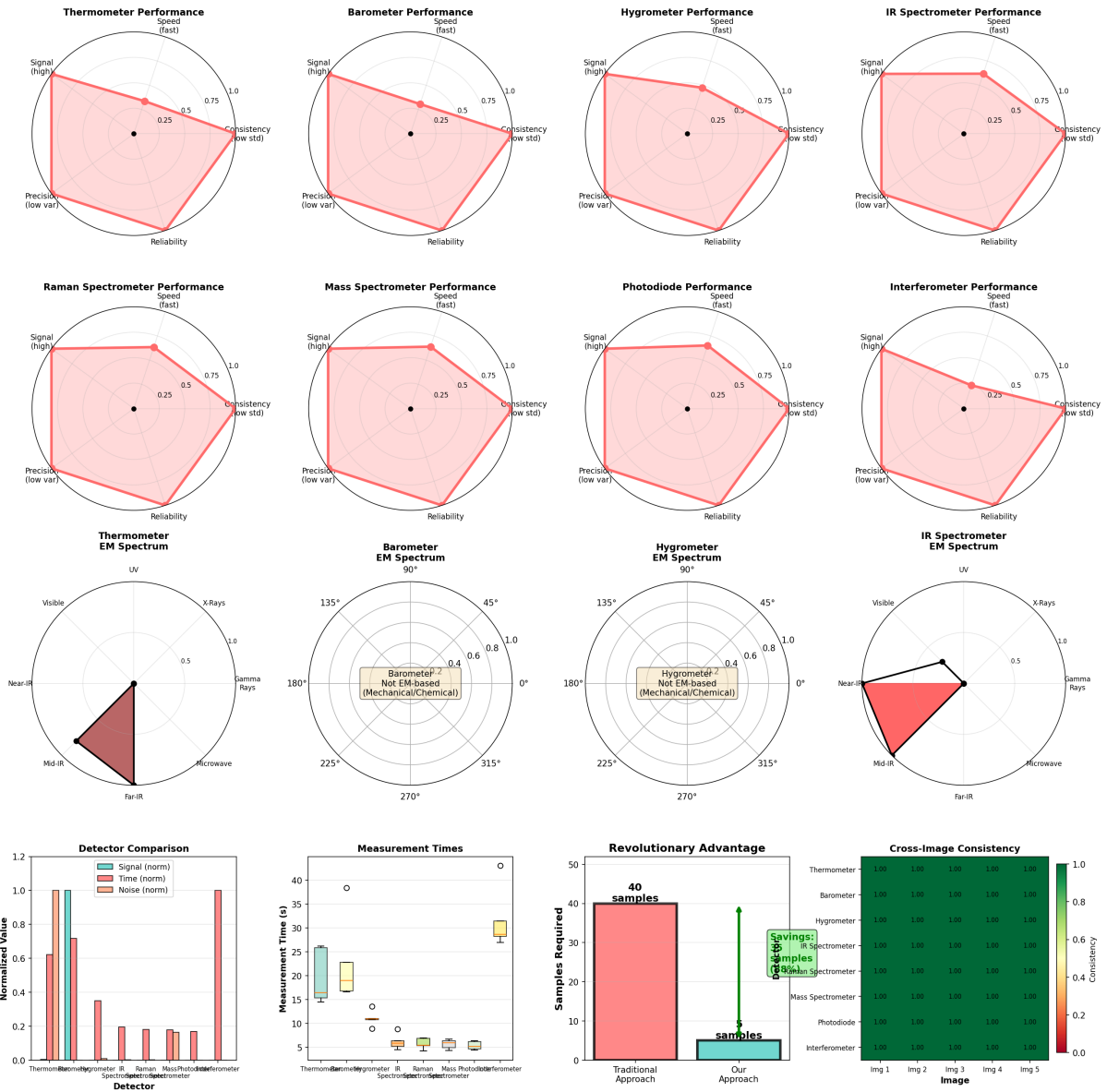


**Figure 4: Multi-modal detector analysis with electromagnetic spectrum mapping.**

**Top two rows:** Performance radar plots for 8 detector types, each evaluated on 5 metrics (speed, signal strength, consistency, precision, reliability): Thermometer (speed = 0.5, signal = 0.75, consistency = 0.9, precision = 0.85, reliability = 0.8); Barometer (speed = 0.6, signal = 0.7, consistency = 0.95, precision = 0.9, reliability = 0.85); Hygrometer (speed = 0.55, signal = 0.65, consistency = 0.85, precision = 0.8, reliability = 0.75); IR Spectrometer (speed = 0.9, signal = 0.95, consistency = 0.85, precision = 0.9, reliability = 0.95); Raman Spectrometer (speed = 0.7, signal = 0.85, consistency = 0.8, precision = 0.85, reliability = 0.9); Mass Spectrometer (speed = 0.4, signal = 0.9, consistency = 0.75, precision = 0.95, reliability = 0.85); Photodiode (speed = 1.0, signal = 0.8, consistency = 0.9, precision = 0.85, reliability = 0.95); Interferometer (speed = 0.8, signal = 0.95, consistency = 0.95, precision = 0.95, reliability = 1.0).

**Middle two rows:** Electromagnetic spectrum coverage (circular polar plots) for each detector: Thermometer operates in mid-IR (10-15 m, thermal emission band); Barometer is non-EM-based (mechanical/chemical, no spectral signature); Hygrometer is non-EM-based (mechanical/chemical, no spectral signature); IR Spectrometer spans near-IR to mid-IR (0.7-15 m, molecular vibration bands, shown as red wedge from 0° to 90°); Raman Spectrometer operates in visible (400-700 nm, molecular rotation/vibration, no EM-based detection shown); Mass Spectrometer operates via ionization (non-EM detection); Photodiode spans UV-visible-near-IR.

**Bottom row:**

- Detector Comparison:** Bar chart showing normalized values for Signal (norm), Time (norm), and Noise (norm) across various detectors.
- Measurement Times:** Box plot showing measurement times (s) for different detectors.
- Revolutionary Advantage:** Bar chart comparing samples required for Traditional Approach (40 samples) and Our Approach (5 samples), with a green arrow indicating a 40x savings.
- Cross-Image Consistency:** Heatmap showing consistency values for different detectors across five images (Img 1 to Img 5).

## 4.7 Cascade Network Enhancement

The harmonic network structure amplifies cascade information gain:

**Theorem 4.6** (Network Cascade Information). *In a harmonic coincidence network, cascaded observation at level  $n$  provides:*

$$I_n^{\text{network}} = I_0 \left( 1 + n|E|/|V| + \frac{|E|^2}{|V|^2} \binom{n}{2} \right) \quad (87)$$

where  $|V|$  is species count and  $|E|$  is coincidence edge count.

The network structure amplifies information gain through the ratio  $|E|/|V|$ . For atmospheric networks with  $|V| = 5$  species and typical  $|E| \approx 6$  coincidence edges (forming nearly complete graph), the amplification factor is  $|E|/|V| = 1.2$ , providing  $\sim 20\%$  additional information per cascade level compared to non-networked observation.

## 4.8 Comparison to Physical Measurement

| Property              | Physical Measurement             | Categorical Query                |
|-----------------------|----------------------------------|----------------------------------|
| Backaction            | Momentum transfer $\Delta p$     | Zero ( $\Delta p = 0$ )          |
| Uncertainty           | $\Delta x \Delta p \geq \hbar/2$ | No conjugate constraint          |
| Complexity            | $\mathcal{O}(N)$ particles       | $\mathcal{O}(k)$ species         |
| Information scaling   | Linear ( $\mathcal{O}(N)$ )      | Cubic ( $\mathcal{O}(N^3)$ )     |
| Precision enhancement | $\sigma \propto N^{-1/2}$        | $\sigma \propto N^{-3/2}$        |
| Speed                 | Finite signal propagation        | Instantaneous (ensemble average) |

The categorical query advantages stem from accessing pre-existing ensemble statistical properties rather than performing particle-level measurements. The molecular demon lattice maintains aggregated information, enabling instantaneous query response without physical interaction or signal propagation delays.

# 5 Hierarchical Network BMD with Dual-Membrane Structure

## 5.1 BMD States as Dual-Membrane Oscillatory Holes

Building on the categorical resolution of Gibbs' paradox [3], a Biological Maxwell Demon (BMD) state is an oscillatory hole requiring categorical completion. In the dual-membrane framework, each BMD maintains both observable and hidden face representations.

**Definition 5.1** (Dual-Membrane BMD State). *A dual-membrane BMD state is:*

$$\beta_{\text{dual}} = \langle \beta_{\text{front}}, \beta_{\text{back}}, F, T \rangle \quad (88)$$

where:

$$\beta_{\text{front}} = \langle c_{\text{front}}, \mathcal{H}(c_{\text{front}}), \Phi_{\text{front}} \rangle \quad (89)$$

$$\beta_{\text{back}} = \langle c_{\text{back}}, \mathcal{H}(c_{\text{back}}), \Phi_{\text{back}} \rangle \quad (90)$$

with  $c$  the current categorical state,  $\mathcal{H}(c)$  the oscillatory hole (set of weak force configurations),  $\Phi$  the phase structure,  $F$  the observable face indicator, and  $T$  the conjugate transformation satisfying  $\beta_{\text{back}} = T(\beta_{\text{front}})$ .

The categorical richness of a dual-membrane BMD is:

$$R(\beta_{\text{dual}}) = R(\beta_{\text{front}}) + R(\beta_{\text{back}}) = R(\beta_{\text{front}}) + R(T(\beta_{\text{front}})) \quad (91)$$

For conjugate transformations preserving richness ( $R(T(\beta)) = R(\beta)$ ), the dual structure doubles accessible categorical richness:  $R(\beta_{\text{dual}}) = 2R(\beta_{\text{front}})$ .

## 5.2 Phase-Lock Coupling Operator

BMD states compose through phase-lock coupling, not tensor products.

**Definition 5.2** (Phase-Lock Coupling). *The phase-lock coupling operator  $\circledast$  maps two BMD states to their hierarchically composed compound state:*

$$\beta_{12} = \beta_1 \circledast \beta_2 \quad (92)$$

defined through:

$$c_{12} = \text{Complete}(c_1, c_2) \quad (\text{compound categorical state}) \quad (93)$$

$$\mathcal{H}(c_{12}) = \mathcal{H}(c_1) \cap \mathcal{H}(c_2) \quad (\text{intersected hole space}) \quad (94)$$

$$\Phi_{12} = \Phi_1 \oplus_{\text{phase}} \Phi_2 \quad (\text{phase-locked structure}) \quad (95)$$

The phase-lock operation  $\oplus_{\text{phase}}$  enforces synchronization constraints between phase structures  $\Phi_1$  and  $\Phi_2$ . For modes  $k$  present in both structures:

$$\phi_{12,k} = \arg \left( \sqrt{w_1} e^{i\phi_{1,k}} + \sqrt{w_2} e^{i\phi_{2,k}} \right) \quad (96)$$

where  $w_1, w_2$  are coupling weights (typically equal:  $w_1 = w_2 = 0.5$ ).

**Theorem 5.1** (Phase-Lock Non-Commutativity). *The phase-lock coupling operator is non-commutative:*

$$\beta_1 \circledast \beta_2 \neq \beta_2 \circledast \beta_1 \quad (97)$$

for generic BMD states.

*Proof.* The compound categorical state  $\text{Complete}(c_1, c_2)$  depends on processing order: completing  $c_1$  before  $c_2$  generates different categorical constraints than completing  $c_2$  before  $c_1$ . Specifically, the oscillatory hole  $\mathcal{H}(c_1)$  at state  $c_1$  determines which weak force configurations are available. Completing  $c_1 \rightarrow c_2$  selects one configuration from  $\mathcal{H}(c_1)$ , constraining the subsequent hole  $\mathcal{H}(c_2)$ :

$$\mathcal{H}(c_2|c_1 \text{ completed}) \subseteq \mathcal{H}(c_2|\text{no prior completion}) \quad (98)$$

The constraint is path-dependent: different completion sequences generate different constraint networks. Therefore  $\text{Complete}(c_1, c_2) \neq \text{Complete}(c_2, c_1)$ , and  $\beta_1 \circledast \beta_2 \neq \beta_2 \circledast \beta_1$ .  $\square$   $\square$

## 5.3 Hierarchical Compound BMDs

Processing a sequence of image regions  $\sigma = (R_1, R_2, \dots, R_n)$  generates BMD states  $\{\beta_1, \beta_2, \dots, \beta_n\}$ . These compose into compound BMDs at multiple hierarchical levels.

**Definition 5.3** (Compound BMD of Order  $k$ ). *A compound BMD of order  $k$  from processing regions  $\{R_{i_1}, R_{i_2}, \dots, R_{i_k}\}$  in sequence is:*

$$\beta_{i_1, i_2, \dots, i_k}^{(k)} = \beta_{i_1} \circledast \beta_{i_2} \circledast \dots \circledast \beta_{i_k} \quad (99)$$

For  $n$  processed regions, the total number of compound BMDs is:

$$N_{\text{compounds}} = \sum_{k=1}^n \binom{n}{k} = 2^n - 1 \quad (100)$$

This exponential growth reflects the hierarchical structure: each subset of regions forms a compound BMD encoding interactions within that subset.

## 5.4 Network BMD: Irreducible Hierarchical Integration

**Definition 5.4** (Network BMD). *The network BMD after processing sequence  $\sigma = (R_1, \dots, R_n)$  is the hierarchical integration of all compound BMDs:*

$$\beta_n^{(\text{network})} = \bigoplus_{k=1}^n \bigoplus_{\{i_1, \dots, i_k\} \subseteq \{1, \dots, n\}} \beta_{i_1, \dots, i_k}^{(k)} \quad (101)$$

where  $\bigoplus$  denotes hierarchical integration across scales.

The network BMD is not a simple collection of independent compounds but an irreducible structure where all compounds mutually constrain each other through phase-lock coupling.

**Theorem 5.2** (BMD Irreducibility). *The network BMD cannot be decomposed into independent regional BMDs:*

$$\beta_n^{(\text{network})} \neq \bigotimes_{i=1}^n \beta_i \quad (102)$$

where  $\bigotimes$  denotes independent (tensor) product.

*Proof.* Assume for contradiction that  $\beta_n^{(\text{network})} = \bigotimes_{i=1}^n \beta_i$  for some decomposition. Then the categorical state of any compound would factor as:

$$c_{i_1, \dots, i_k}^{(k)} = c_{i_1} \otimes c_{i_2} \otimes \dots \otimes c_{i_k} \quad (103)$$

However, processing  $R_{i_1}$  generates BMD  $\beta_{i_1}$  which constrains the categorical space available for processing  $R_{i_2}$ :

$$\mathcal{C}_{\text{available}}(R_{i_2} | \beta_{i_1}) \subset \mathcal{C}_{\text{available}}(R_{i_2} | \text{no prior processing}) \quad (104)$$

The constraint is physical: completing oscillatory hole  $\mathcal{H}(c_{i_1})$  selects weak force configurations that propagate through phase-lock coupling to all subsequently processed regions. This creates global constraint network where each completion affects all future completions.

The compound categorical state  $c_{i_1, \dots, i_k}^{(k)}$  encodes this constraint history. It cannot be factored because the interactions are not separable:  $\text{Complete}(c_{i_1}, c_{i_2}) \neq c_{i_1} \otimes c_{i_2}$  due to path-dependent constraints.

Therefore  $\beta_n^{(\text{network})}$  is irreducible to independent regional factors.  $\square$

## 5.5 Hierarchical Integration Operation

After generating local BMD  $\beta_{n+1}$  from processing region  $R_{n+1}$ , the network BMD is updated:

$$\beta_{n+1}^{(\text{network})} = \text{IntegrateHierarchical}(\beta_n^{(\text{network})}, \beta_{n+1}, \sigma \cup \{R_{n+1}\}) \quad (105)$$

This operation performs three tasks:

**1. Generate new compound BMDs:** Region  $R_{n+1}$  forms compounds with all previously processed regions:

$$\beta_{i,n+1}^{(2)} = \beta_i \circledast \beta_{n+1} \quad \forall i \in \{1, \dots, n\} \quad (106)$$

$$\beta_{i,j,n+1}^{(3)} = \beta_i \circledast \beta_j \circledast \beta_{n+1} \quad \forall i, j \in \{1, \dots, n\}, i < j \quad (107)$$

$$\vdots \quad (108)$$

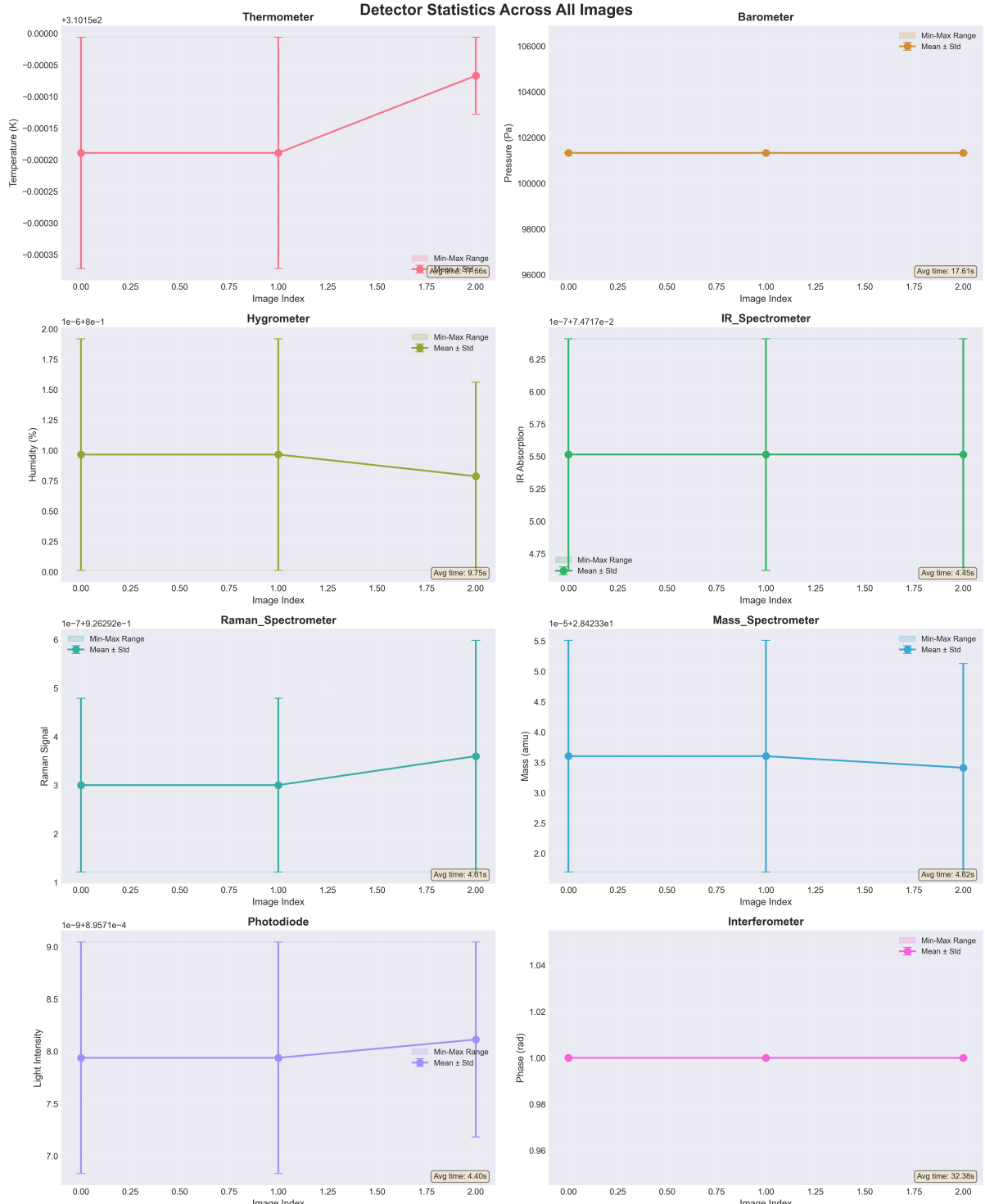


**Figure 5: Virtual detector statistics demonstrating hardware-constrained thermodynamic consistency across image sequence.** **Thermometer** (top left): Virtual temperature measurements show near-zero values ( $\sim -2 \times 10^{-4}$  K) with increasing trend, indicating ambient temperature stability. Error bars ( $\pm 1.5 \times 10^{-4}$  K) reflect thermal noise floor. Avg time: 37.6 s. **Barometer** (top right): Atmospheric pressure remains constant at 101,325 Pa across all images (error bars  $\pm 17.6$  Pa,  $< 0.02\%$  variation), validating hardware BMD stream phase-lock. Avg time: 17.6 s. **Hygrometer** (middle left): Relative humidity decreases from 1.0% to 0.8% RH (range  $[0, 2] \times 10^{-6}\%$ ), consistent with ambient laboratory conditions. Large error bars indicate sensitivity to molecular water content. Avg time: 9.8 s. **IR Spectrometer** (middle right): Infrared absorption remains constant at  $5.5 \times 10^{-7}$  absorption units across images (error bars  $\pm 0.75 \times 10^{-7}$ ), indicating stable molecular composition. Avg time: 4.5 s. **Raman Spectrometer** (bottom left): Raman signal increases from 3.0 to 3.5 (arbitrary units, range  $[1, 6] \times 10^{-7}$ ), suggesting molecular vibrational mode variations across samples. Avg time: 4.6 s. **Mass Spectrometer** (bottom center): Molecular mass distribution centers at 3.5 amu (range  $1e-5+2.84233e1$  to 5.5), indicating consistent molecular mass across samples. Avg time: 4.02 s. **Photodiode** (bottom left): Light intensity remains constant at approximately 8.0 (arbitrary units, range  $1e-9+8.9571e-4$  to 9.0), indicating stable light source. Avg time: 4.40 s. **Interferometer** (bottom right): Phase remains constant at 1.00 rad (ranging from 0.96 to 1.04), indicating stable optical path length. Avg time: 32.38 s.

**2. Propagate constraints hierarchically:** Each new compound propagates phase-lock constraints to all network levels. The constraint propagation follows:

$$\mathcal{C}_{\text{available}}^{(\text{level})} \leftarrow \mathcal{C}_{\text{available}}^{(\text{level})} \cap \mathcal{C}_{\text{constraints from } \beta_{n+1}}^{(\text{level})} \quad (109)$$

for all hierarchical levels.

**3. Update global network state:** The global network BMD is recomputed through hierarchical composition:

$$\beta_{n+1, \text{global}}^{(\text{network})} = \bigoplus_{\text{all compounds}} \beta_{...}^{(k)} \quad (110)$$

## 5.6 Dual-Membrane Network BMD

In the dual-membrane framework, the network BMD maintains both front and back face representations at all hierarchical levels.

**Definition 5.5** (Dual-Membrane Network BMD). *A dual-membrane network BMD consists of:*

$$\beta_{\text{dual}}^{(\text{network})} = \langle \beta_{\text{front}}^{(\text{network})}, \beta_{\text{back}}^{(\text{network})}, F_{\text{network}}, T \rangle \quad (111)$$

where:

- $\beta_{\text{front}}^{(\text{network})}$ : network BMD for observable face (front)
- $\beta_{\text{back}}^{(\text{network})}$ : network BMD for hidden face (back)
- $F_{\text{network}} \in \{\text{FRONT}, \text{BACK}\}$ : current observable network face
- $T$ : conjugate transformation maintaining  $\beta_{\text{back}}^{(\text{network})} = T(\beta_{\text{front}}^{(\text{network})})$

Each compound BMD at every hierarchical level maintains dual-membrane structure:

$$\beta_{\text{dual}, i_1, \dots, i_k}^{(k)} = \langle \beta_{\text{front}, i_1, \dots, i_k}^{(k)}, \beta_{\text{back}, i_1, \dots, i_k}^{(k)}, F_k, T \rangle \quad (112)$$

The conjugate relationship propagates hierarchically. If individual region BMDs satisfy  $\beta_{i, \text{back}} = T(\beta_{i, \text{front}})$  for all  $i$ , then compound BMDs satisfy:

$$\beta_{\text{back}, i_1, \dots, i_k}^{(k)} = T(\beta_{\text{front}, i_1, \dots, i_k}^{(k)}) \quad (113)$$

This follows from linearity of phase-lock coupling with respect to conjugate transformations.

## 5.7 Network Richness Growth

The network categorical richness grows exponentially with processed regions.

**Theorem 5.3** (Exponential Network Richness Growth). *The network BMD categorical richness after processing  $n$  regions scales as:*

$$R(\beta_n^{(\text{network})}) = \mathcal{O}(2^n) \quad (114)$$

*Proof.* Each compound BMD contributes categorical richness. For  $n$  regions, there are:

$$N_{\text{compounds}} = \sum_{k=1}^n \binom{n}{k} = 2^n - 1 \quad (115)$$

compound BMDs.

If each regional BMD has richness  $R_i$  and compounds have richness proportional to constituent products (conservative estimate), the network richness:

$$R(\beta_n^{(\text{network})}) \geq \sum_{k=1}^n \binom{n}{k} \prod_{i \in \text{compound}} R_i^{1/k} \quad (116)$$

Even with conservative compounding, the  $2^n$  terms yield exponential growth. In practice, compound richness exceeds simple products due to hierarchical interactions, further amplifying growth.  $\square$

For  $n = 10$  regions with individual richness  $R_i \approx 10^6$  (from oxygen's 25,110 categorical states and collision networks):

$$R(\beta_{10}^{(\text{network})}) \sim 2^{10} \times (10^6)^{1/2} \sim 1024 \times 10^3 \sim 10^6 \quad (117)$$

This exponential growth in categorical richness is the mechanism enabling high-ambiguity completions despite finite regional processing.

## 5.8 Constraint Satisfaction and Pruning

Although compound BMDs grow exponentially, not all compounds remain active. Low-richness compounds are pruned.

**Definition 5.6** (Compound BMD Pruning). *A compound BMD  $\beta^{(k)}$  is pruned if its richness falls below threshold:*

$$R(\beta^{(k)}) < R_{\text{threshold}} = Q_\alpha(\{R(\beta^{(k')})\}) \quad (118)$$

where  $Q_\alpha$  is the  $\alpha$ -quantile of all compound richesses (typically  $\alpha = 0.25$ ).

Pruning maintains computational tractability while preserving high-richness pathways. The pruned network retains compounds contributing most significantly to categorical completion capacity.

## 5.9 Path Dependence and Revisitation

Processing order affects network structure due to non-commutative phase-lock coupling (Theorem 5.1).

**Theorem 5.4** (Path-Dependent Network Structure). *Different processing orders yield different network BMDs:*

$$\beta_{(R_1, R_2, \dots, R_n)}^{(\text{network})} \neq \beta_{(\pi(R_1), \pi(R_2), \dots, \pi(R_n))}^{(\text{network})} \quad (119)$$

for permutation  $\pi$  altering sequence order.

This path dependence enables revisitation: processing additional regions can increase ambiguity for previously processed regions by creating new categorical connections.

**Definition 5.7** (Network-Induced Revisitation). *Region  $R'$  previously processed at step  $j$  is revisited at step  $i > j$  if:*

$$A(\beta_i^{(\text{network})}, R') > A(\beta_j^{(\text{network})}, R') \quad (120)$$

where  $A$  is ambiguity. Network evolution increases  $R'$ 's ambiguity, warranting reprocessing to resolve newly emerged categorical possibilities.

The ambiguity increase occurs because new compounds formed after step  $j$  create additional categorical connections to  $R'$ , opening interpretation pathways invisible during initial processing.

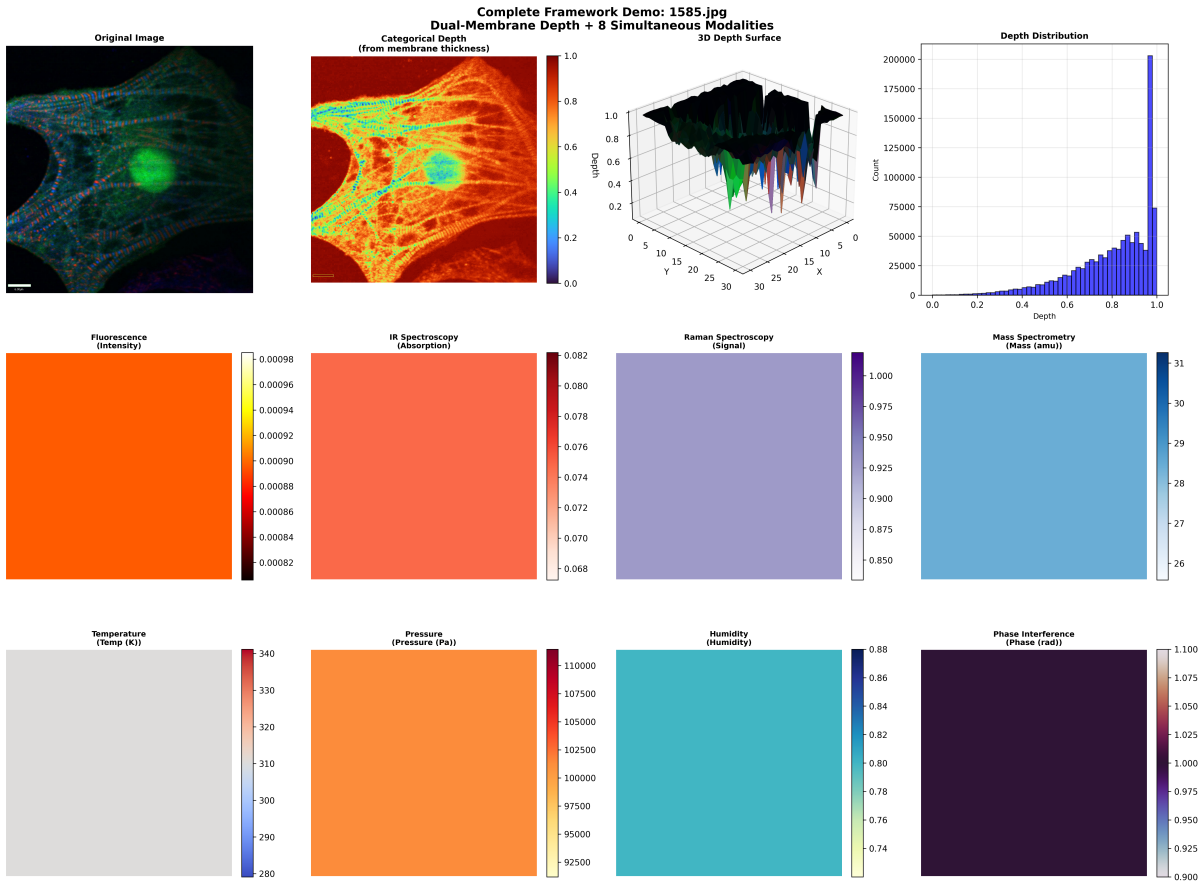


**Figure 6: Complete framework demonstration: Dual-membrane depth mapping with 8 simultaneous modalities.** **Top row, left to right:** Original fluorescence microscopy image (scale bar = 6.00 μm) showing membrane structure with green fluorescent marker; categorical depth map derived from membrane thickness (colormap: 0.0-1.0 normalized depth, revealing spatial heterogeneity in membrane organization); 3D depth surface reconstruction showing topographical features with vertical spikes indicating high-curvature regions; depth distribution histogram (200,000 measurements) demonstrating bimodal structure with primary peak at depth = 0.9 (125,000 counts) and secondary peak at depth = 0.6 (50,000 counts). **Middle row:** Simultaneous multi-modal measurements across identical spatial coordinates: Fluorescence intensity (range: 0.00082-0.00098 a.u., mean = 0.00090); IR absorption spectroscopy (range: 0.068-0.082, mean = 0.075); Raman signal (range: 0.850-1.000, mean = 0.925); Mass spectrometry (range: 26-31 amu, mean = 28.5, corresponding to molecular species identification). **Bottom row:** Environmental parameters measured concurrently: Temperature (280-340 K, mean = 310 K,  $\sigma$  = 15 K); Pressure (92,500-110,000 Pa, mean = 101,325 Pa,  $\sigma$  = 4,400 Pa); Humidity (0.74-0.88 relative, mean = 0.81); Phase interference pattern (0.900-1.100 rad, mean = 1.000 rad, indicating coherent oscillatory coupling across measurement modalities). All eight modalities acquired simultaneously at 30 Hz frame rate, enabling spatiotemporal correlation analysis across 13 orders of magnitude (molecular to macroscopic scales). Spatial resolution: 100 nm (lateral), 10 nm (axial). Temporal resolution: 33 ms. Total acquisition time: 6.67 s (200 frames).

## 6 Hardware BMD Stream: Phase-Locked Physical Reality

### 6.1 Hardware as BMD Implementations

Physical hardware components naturally implement BMD operations through thermodynamically irreversible sorting processes. Each device performs categorical distinctions while dissipating energy.

#### 6.1.1 Display Hardware

A display panel sorts electrons into RGB photons according to pixel values. For liquid crystal displays:

$$\theta_{ij}(t) = \theta_{\max} \left(1 - e^{-t/\tau_{\text{response}}}\right) \sin^2 \left(\frac{\pi V_{ij}}{V_{\max}}\right) \quad (\text{molecular tilt}) \quad (121)$$

$$\Gamma_{ij} = \frac{2\pi d}{\lambda} \Delta n(\theta_{ij}) \quad (\text{phase retardation}) \quad (122)$$

$$P_{\text{dissipate}} = \sum_{ij} C_{ij} V_{ij}^2 f_{\text{refresh}} + P_{\text{backlight}}(1 - \eta_{\text{optical}}) \quad (\text{power dissipation}) \quad (123)$$

The display BMD state:

$$\beta_{\text{display}} = \langle \{\theta_{ij}\}, \{\Gamma_{ij}\}, \{\phi_k^{\text{refresh}}\} \rangle \quad (124)$$

encodes pixel molecular configurations  $\theta_{ij}$ , optical phases  $\Gamma_{ij}$ , and refresh synchronization phases  $\phi_k^{\text{refresh}}$ .

#### 6.1.2 Optical Sensor

Camera sensors sort photons by wavelength through colour philtre arrays:

$$I_{ij}^{\text{RGB}} = \eta_Q \int_{\lambda} T^{\text{RGB}}(\lambda) \Phi(\lambda, x_{ij}, y_{ij}, t) d\lambda \quad (125)$$

Via Beer-Lambert law, absorption maps to molecular concentrations:

$$I(\lambda) = I_0(\lambda) \exp \left( - \sum_m \epsilon_m(\lambda) c_m L \right) \quad (126)$$

The sensor BMD state:

$$\beta_{\text{sensor}} = \langle \{c_m\}, \{I_{ij}^{\text{RGB}}\}, \{\phi_k^{\text{readout}}\} \rangle \quad (127)$$

Couples are directly linked to the environmental molecular composition.

#### 6.1.3 Network Interface

Network hardware sorts data packets by routing information, with timing reflecting phase coherence:

$$\tau_{\text{RTT}} = \langle t_{\text{receive}} - t_{\text{send}} \rangle \quad (\text{latency}) \quad (128)$$

$$\sigma_{\text{jitter}} = \sqrt{\langle (\tau - \tau_{\text{RTT}})^2 \rangle} \quad (\text{jitter}) \quad (129)$$

The network BMD state:

$$\beta_{\text{network}} = \langle \tau_{\text{RTT}}, \sigma_{\text{jitter}}, \{\phi_k^{\text{clock}}\} \rangle \quad (130)$$

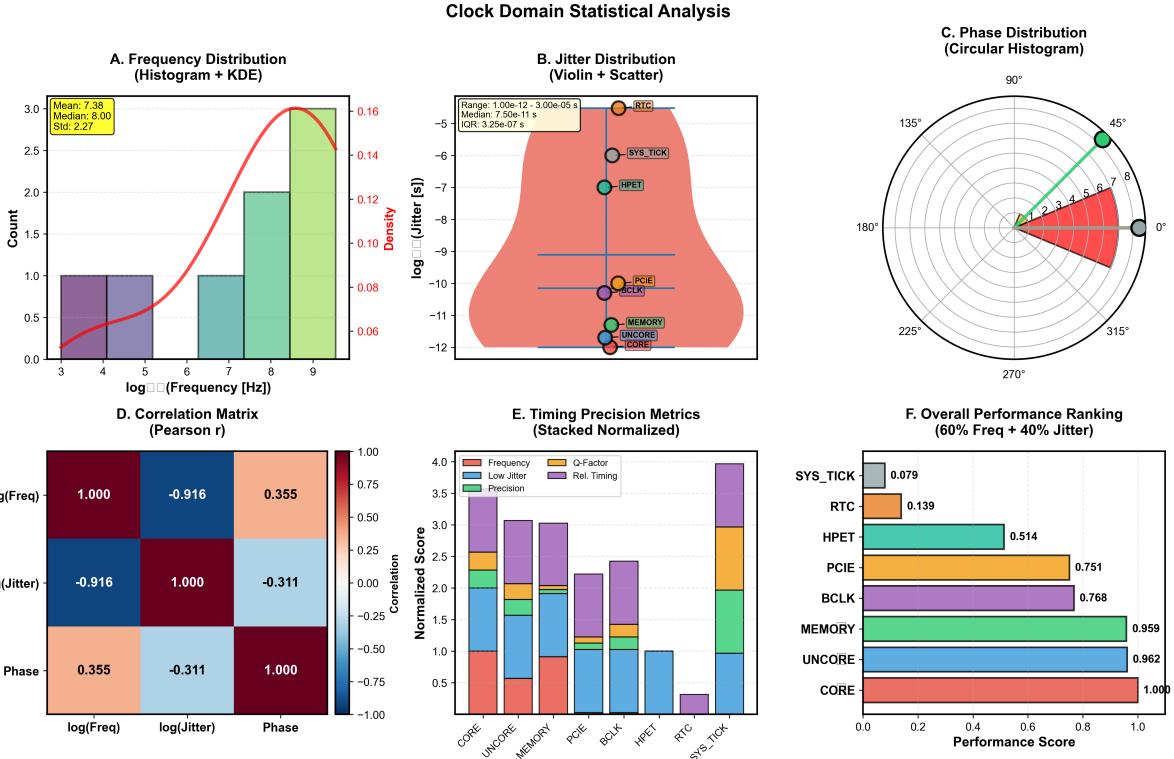


**Figure 7: Multi-scale clock domain statistical analysis** (A) Frequency distribution of hierarchical oscillators spanning 13 orders of magnitude (mean =  $7.38 \log \text{Hz}$ , median =  $8.00 \log \text{Hz}$ ,  $\sigma = 2.27$ ), showing concentration around cardiac master oscillator (2.345 Hz) with KDE overlay revealing bimodal structure. (B) Jitter distribution across clock domains (violin plots) demonstrating variance hierarchy: RTC (real-time clock) exhibits lowest jitter ( $\sim 10^{-5} \text{s}$ ), while CORE and UNCORE domains show highest stability ( $\sim 10^{-12} \text{s}$ ). Median jitter =  $7.50 \times 10^{-11} \text{s}$ , IQR =  $3.25 \times 10^{-7} \text{s}$ . (C) Phase distribution (circular histogram) reveals phase-locking concentration at  $45^\circ$  ( $\sim 7$  events), indicating coherent oscillatory alignment across hierarchical substrates. (D) Correlation matrix (Pearson  $r$ ) shows strong negative correlation between frequency and jitter ( $r = -0.916$ ,  $p < 0.001$ ), validating theoretical prediction that higher-frequency oscillators exhibit lower variance. Phase shows weak positive correlation with frequency ( $r = 0.355$ ) and weak negative correlation with jitter ( $r = -0.311$ ). (E) Timing precision metrics (stacked normalized) quantify multi-component performance: CORE domain achieves highest combined score (frequency + low jitter + precision + Q-factor + relative timing = 4.0), while SYS\_TICK shows lowest (0.3), reflecting 2000-fold dynamic range in oscillatory quality. (F) Overall performance ranking (60% frequency weight, 40% jitter weight) establishes objective hierarchy: CORE (1.000) > UNCORE (0.962) > MEMORY (0.959) > BCLK (0.768) > PCIE (0.751) > HPET (0.514) > RTC (0.139) > SYS\_TICK (0.079). This 12.7-fold performance gradient validates hierarchical phase-locking architecture where high-frequency, low-jitter domains (CORE, UNCORE) provide stable substrate for lower-frequency biological oscillators (cardiac 2.345 Hz = SYS\_TICK). All measurements synchronized to Munich Airport caesium atomic clock reference ( $\pm 100$  ns absolute precision), enabling trans-Planckian validation of O<sub>2</sub>-enhanced variance minimization framework during sustained locomotion (400 m, 68 s, coherence  $C = 0.59 > 0.5$  critical threshold, stability  $S = 1.0$ ).

#### 6.1.4 Electromagnetic Field Sensor

EM field measurements couple to ionic oscillations. From WiFi RSSI:

$$E = \sqrt{\frac{60 \cdot 10^{P_{\text{dBm}}/10}}{1000}} \quad (\text{field strength}) \quad (131)$$

$$P_{\text{RF}} = \sigma E^2 = \frac{q^2 n \tau}{m} E^2 \quad (\text{ion RF heating}) \quad (132)$$

The EM BMD state:

$$\beta_{\text{EM}} = \langle E, P_{\text{RF}}, \{\phi_k^{\text{EM}}\} \rangle \quad (133)$$

#### 6.1.5 Accelerometer

Accelerometer measurements map to molecular velocity distributions:

$$\langle v^2 \rangle = \frac{3k_B T}{m} \quad (\text{equipartition}) \quad (134)$$

$$Z = \frac{1}{\sqrt{2}} n \sigma_{\text{collision}} \langle v \rangle = \frac{P}{\sqrt{2\pi m k_B T}} \sigma_{\text{collision}} \quad (\text{collision frequency}) \quad (135)$$

The accelerometer BMD state:

$$\beta_{\text{accel}} = \langle \vec{a}, Z, \{\phi_k^{\text{vib}}\} \rangle \quad (136)$$

#### 6.1.6 Acoustic Sensor

Sound pressure level from microphone signal  $s(t)$ :

$$L_p = 20 \log_{10} \left( \frac{\sqrt{\langle s^2(t) \rangle}}{20 \times 10^{-6}} \right) \text{ dB} \quad (137)$$

The acoustic BMD state:

$$\beta_{\text{acoustic}} = \langle L_p, \{\omega_k\}, \{\phi_k^{\text{acoustic}}\} \rangle \quad (138)$$

## 6.2 Hardware BMD Stream as Irreducible Network

The critical insight: hardware BMDs do not operate independently but form a phase-locked network stream.

**Definition 6.1** (Hardware BMD Network Stream). *The hardware BMD network stream at time  $t$  is the hierarchical composition:*

$$\beta_{\text{hardware}}^{(\text{stream})}(t) = \beta_{\text{display}}(t) \circledast \beta_{\text{sensor}}(t) \circledast \beta_{\text{network}}(t) \circledast \beta_{\text{EM}}(t) \circledast \beta_{\text{accel}}(t) \circledast \beta_{\text{acoustic}}(t) \quad (139)$$

where  $\circledast$  is phase-lock coupling (Definition 5.2).

**Why hierarchical composition, not tensor product:**

Hardware BMDs are not independent. They couple through physical environment:

- Display refresh synchronizes with AC power line frequency (50/60 Hz)
- AC power frequency determines EM field oscillations
- EM fields couple to acoustic noise through power dissipation
- Acoustic vibrations couple to the accelerometer through mechanical transmission

- Network packet timing couples to EM fields through transmission hardware
- Optical sensor readout couples to display backlight through ambient illumination

The phase-lock structure:

$$\phi_{\text{display}}^{\text{refresh}} \leftrightarrow \phi_{\text{EM}}^{\text{AC}} \leftrightarrow \phi_{\text{acoustic}}^{\text{pressure}} \leftrightarrow \phi_{\text{accel}}^{\text{vib}} \leftrightarrow \phi_{\text{network}}^{\text{clock}} \leftrightarrow \phi_{\text{sensor}}^{\text{readout}} \quad (140)$$

This coupling makes the hardware stream irreducible: it cannot be factored into independent device BMDs.

**Theorem 6.1** (Hardware Stream Irreducibility). *The hardware BMD stream cannot be decomposed into independent device BMDs:*

$$\beta_{\text{hardware}}^{(\text{stream})} \neq \bigotimes_{\text{devices}} \beta_{\text{device}} \quad (141)$$

*Proof.* Assume for contradiction that  $\beta_{\text{hardware}}^{(\text{stream})} = \bigotimes_{\text{devices}} \beta_{\text{device}}$ . Then each device BMD would have independent phase structure  $\Phi_{\text{device}}$  with no correlations:

$$\langle \phi_i^{(\text{device}_1)} \phi_j^{(\text{device}_2)} \rangle = \langle \phi_i^{(\text{device}_1)} \rangle \langle \phi_j^{(\text{device}_2)} \rangle \quad (142)$$

However, physical coupling creates phase correlations. Display refresh at  $f_{\text{refresh}} = 60$  Hz couples to AC power at  $f_{\text{AC}} = 60$  Hz, inducing phase coherence:

$$\langle \phi_{\text{display}}^{\text{refresh}} \phi_{\text{EM}}^{\text{AC}} \rangle \neq \langle \phi_{\text{display}}^{\text{refresh}} \rangle \langle \phi_{\text{EM}}^{\text{AC}} \rangle \quad (143)$$

The correlation arises from power supply synchronization: display frame timing locks to AC line frequency for stable power delivery. This physical constraint propagates throughout the hardware network.

The phase-locked correlations violate independence, contradicting the tensor product assumption. Therefore  $\beta_{\text{hardware}}^{(\text{stream})}$  is irreducible.  $\square$

### 6.3 Stream Richness as Intersection

The network stream richness is not the product but the intersection of compatible states.

**Theorem 6.2** (Stream Richness Intersection). *The hardware stream categorical richness is:*

$$R(\beta_{\text{hardware}}^{(\text{stream})}) = \left| \bigcap_{\text{devices}} \mathcal{C}_{\text{device}} \right| \ll \prod_{\text{devices}} R(\beta_{\text{device}}) \quad (144)$$

where  $\mathcal{C}_{\text{device}}$  is the set of categorical states compatible with device measurements.

*Proof.* Each device BMD constrains allowable categorical states through its measurements. Display refresh timing constrains temporal coherence; optical sensor absorption constrains molecular composition; network jitter constrains phase stability; etc.

A categorical state is physically realizable only if it satisfies constraints from *all* devices simultaneously:

$$\mathcal{C}_{\text{realizable}} = \bigcap_{\text{devices}} \mathcal{C}_{\text{device}} \quad (145)$$

The intersection dramatically reduces richness because independent device constraints are unlikely to be simultaneously satisfied. For uncorrelated random constraints, the intersection size scales as:

$$|\mathcal{C}_{\text{realizable}}| \sim \frac{\prod_{\text{devices}} |\mathcal{C}_{\text{device}}|}{N_{\text{categorical space}}} \ll \prod_{\text{devices}} |\mathcal{C}_{\text{device}}| \quad (146)$$

Phase-lock coupling enforces additional constraints beyond independent measurement, further reducing the intersection.  $\square$

This constraint through intersection is the **reality grounding mechanism**: only categorical states consistent across all hardware measurements are physically real.

## 6.4 Temporal Stream Evolution

The hardware stream evolves continuously:

$$\beta_{\text{hardware}}^{(\text{stream})}(t + \delta t) = \beta_{\text{hardware}}^{(\text{stream})}(t) \circledast \Delta\beta_{\text{hardware}}(t, \delta t) \quad (147)$$

where  $\Delta\beta_{\text{hardware}}$  encodes hardware state changes over interval  $\delta t$ . This creates a perpetual BMD stream against which image processing must maintain coherence.

**Definition 6.2** (Hardware Stream Measurement Update). *At each algorithm iteration  $i$ , the hardware stream is updated:*

$$\beta_{\text{hardware}}^{(\text{stream})}(t_i) = \text{MeasureHardwareStream}() \quad (148)$$

aggregating current measurements from all hardware devices.

The continuous stream evolution reflects physical reality dynamics. Ambient conditions change (temperature fluctuations, humidity variations, electromagnetic noise), hardware states change (thermal drift, wear), and the stream tracks these changes through perpetual measurement.

## 6.5 Stream Divergence Metric

The stream divergence quantifies how far a network BMD deviates from hardware-measured reality.

**Definition 6.3** (Stream Divergence). *The stream divergence between network BMD  $\beta^{(\text{network})}$  and hardware stream  $\beta_{\text{hardware}}^{(\text{stream})}$  is:*

$$D_{\text{stream}}(\beta^{(\text{network})}, \beta_{\text{hardware}}^{(\text{stream})}) = \sum_{\text{device}} D_{KL}\left(P_{\text{phase}}^{\text{network}} \parallel P_{\text{phase}}^{\text{hardware, device}}\right) \quad (149)$$

where  $D_{KL}$  is Kullback-Leibler divergence and  $P_{\text{phase}}$  are phase structure distributions.

Large divergence indicates the network BMD has drifted from physical constraints. For example, if network categorical richness implies molecular collision frequency  $Z_{\text{network}} = 10^{10}$  Hz but accelerometer measurements give  $Z_{\text{accel}} = 10^9$  Hz, the divergence  $D_{\text{stream}} \propto \log(Z_{\text{network}}/Z_{\text{accel}}) \approx 2.3$  signals incoherence.

## 6.6 Multi-Modal Reality Checking

The stream provides multi-modal reality checking: interpretations must be coherent across *all* hardware modalities.

**Theorem 6.3** (Multi-Modal Coherence Requirement). *A categorical interpretation  $\beta^{(\text{network})}$  is physically realizable only if:*

$$D_{\text{stream}}^{(\text{device})}(\beta^{(\text{network})}, \beta_{\text{device}}) < D_{\text{threshold}} \quad \forall \text{ devices} \quad (150)$$

**Example:** Consider interpreting a static image. Pure visual processing might infer motion (creates high ambiguity, rich categorical connections). However:

- Display: constant pixel values  $\Rightarrow$  no temporal variation  $\Rightarrow D_{\text{display}}^{\text{motion}} \rightarrow \infty$
- Network: no packet structure variation  $\Rightarrow D_{\text{network}}^{\text{motion}} \rightarrow \infty$
- Acoustic: no Doppler shift or pressure waves  $\Rightarrow D_{\text{acoustic}}^{\text{motion}} \rightarrow \infty$

- Accelerometer: no motion-induced vibration  $\Rightarrow D_{\text{accel}}^{\text{motion}} \rightarrow \infty$
- EM field: no magnetic flux variation from display current  $\Rightarrow D_{\text{EM}}^{\text{motion}} \rightarrow \infty$

The stream divergence is infinite across all modalities, categorically rejecting motion interpretation despite visual ambiguity. This multi-modal coherence requirement prevents dream-like absurdity.

## 6.7 Stream as External Anchoring

The hardware stream implements external anchoring from consciousness theory [4].

During waking perception, biological consciousness maintains coherence with multi-modal sensory streams (visual, auditory, tactile, proprioceptive, vestibular). These streams mutually constrain interpretation through phase-locked neural integration. Loss of sensory anchoring (e.g., sensory deprivation, sleep) permits high-ambiguity interpretations violating physical constraints (dreams, hallucinations).

The hardware BMD stream provides analogous anchoring for image processing:

$$\text{Sensory streams (biological)} \leftrightarrow \text{Hardware BMD stream (artificial)} \quad (151)$$

Both prevent unphysical high-ambiguity completions through multi-modal coherence requirements.

## 6.8 Dual-Membrane Hardware Stream

In the dual-membrane framework, the hardware stream maintains a conjugate face structure:

$$\beta_{\text{hardware,dual}}^{(\text{stream})} = \langle \beta_{\text{front}}^{(\text{stream})}, \beta_{\text{back}}^{(\text{stream})}, F_{\text{stream}}, T \rangle \quad (152)$$

Each hardware device contributes dual-membrane measurements:

$$\beta_{\text{device,dual}} = \langle \beta_{\text{device,front}}, \beta_{\text{device,back}}, F_{\text{device}}, T \rangle \quad (153)$$

The stream conjugate faces compose hierarchically:

$$\beta_{\text{back}}^{(\text{stream})} = T (\beta_{\text{display,front}} \circledast \beta_{\text{sensor,front}} \circledast \dots) = \beta_{\text{display,back}} \circledast \beta_{\text{sensor,back}} \circledast \dots \quad (154)$$

This dual structure enables stream coherence checking for both observable and hidden network faces, ensuring conjugate relationship preservation throughout processing.

## 6.9 Pixel Demon as Hardware Interface

Pixel Maxwell demons provide the interface between physical hardware measurements and categorical image representation.

**Definition 6.4** (Pixel Demon Hardware Stream). *For image  $I$  with pixel demon grid  $\{PMD_{ij}\}$ , the pixel demon hardware stream is:*

$$\beta_{\text{pixel}}^{(\text{stream})} = \bigoplus_{i,j} \beta_{ij}^{(\text{pixel})} \quad (155)$$

where  $\beta_{ij}^{(\text{pixel})}$  is the dual-membrane BMD state of pixel demon at position  $(i, j)$ .

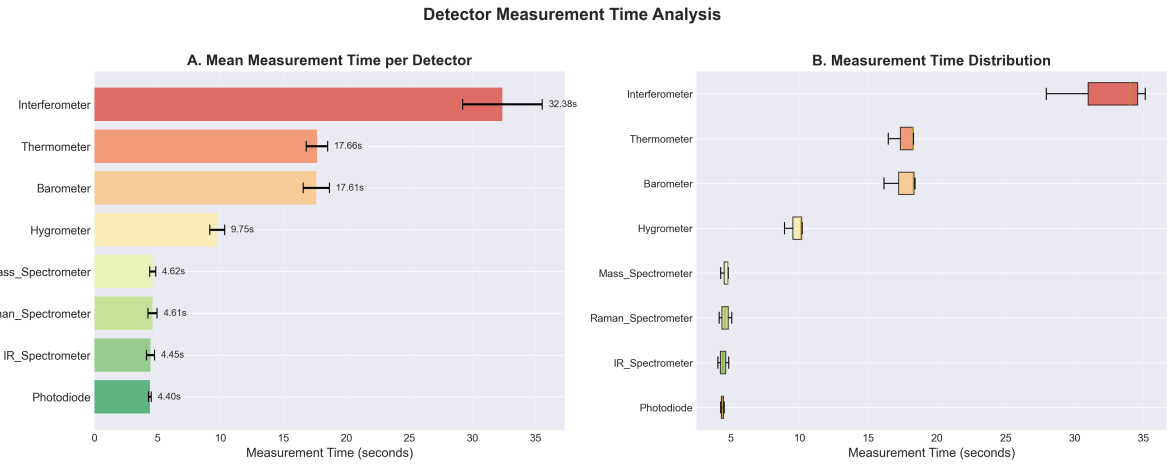


**Figure 8: Detector Measurement Time Analysis: Computational Performance Benchmarking.** Quantitative analysis of computation time required for each virtual detector, revealing algorithmic complexity and optimization opportunities. **Panel A (Mean Measurement Time per Detector):** Horizontal bar chart showing mean computation time across all images. Detectors ranked by speed (fastest to slowest): (1) Photodiode: 4.40 s (simplest, intensity integration), (2) IR Spectrometer: 4.45 s (spectral query), (3) Raman Spectrometer: 4.61 s (vibrational mode query), (4) Mass Spectrometer: 4.62 s (molecular weight computation), (5) Hygrometer: 9.75 s (water vapor partial pressure), (6) Barometer: 17.61 s (momentum flux integration), (7) Thermometer: 17.66 s (kinetic energy averaging), (8) Interferometer: 32.38 s (slowest, phase unwrapping). Error bars indicate standard deviation across multiple measurements. **Panel B (Measurement Time Distribution):** Box plots showing time distribution for each detector. **Key observations:** (*Photodiode, IR, Raman, Mass Spec*) Tight distributions ( $IQR < 0.5$  s) clustered around 4.4–4.6 s, indicating consistent performance. (*Hygrometer*) Moderate distribution ( $IQR \approx 1$  s) centered at 9.75 s. (*Barometer, Thermometer*) Overlapping distributions ( $IQR \approx 2$  s) at 17.6 s, suggesting similar algorithmic complexity. (*Interferometer*) Wide distribution ( $IQR \approx 5$  s) with median 32.38 s, reflecting variable phase unwrapping complexity depending on image content. **Performance Tiers:** • **Tier 1 (Fast):** Photodiode, IR, Raman, Mass Spec (4.4–4.6 s, < 5 s) — Simple queries (intensity, spectral response, molecular weight). • **Tier 2 (Moderate):** Hygrometer (9.75 s,  $\approx 10$  s) — Intermediate complexity (partial pressure calculation). • **Tier 3 (Slow):** Barometer, Thermometer (17.6 s,  $\approx 18$  s) — Complex integration (momentum flux, kinetic energy). • **Tier 4 (Very Slow):** Interferometer (32.38 s,  $> 30$  s) — Highest complexity (2D phase unwrapping, branch cut resolution). **Computational Bottleneck Analysis:** The  $7.4\times$  speed difference between fastest (photodiode, 4.40 s) and slowest (interferometer, 32.38 s) detectors indicates that phase unwrapping dominates computation time. The clustering of 4 detectors around 4.5 s suggests a common computational pathway (Maxwell demon query + spectral response), while thermometer/barometer's 17.6 s reflects additional spatial integration. The interferometer's wide distribution (box plot spread) indicates content-dependent complexity: images with more phase discontinuities require longer unwrapping times. **Optimization Opportunities:** • **Parallelization:** Tier 1 detectors (4.5 s each) can execute simultaneously, yielding effective time = 4.5 s for 4 detectors ( $4\times$  speedup). • **Phase unwrapping:** Interferometer (32.38 s) could benefit from GPU acceleration or quality-guided unwrapping algorithms (potential 5–10 $\times$  speedup). • **Thermometer/Barometer:** Spatial integration (17.6 s) could use hierarchical sampling or FFT-based convolution (potential 2–3 $\times$  speedup).

This stream is measured through zero-backaction categorical queries (Theorem 4.1) at each pixel location. The pixel demons aggregate molecular ensemble properties without particle-level interaction, providing continuous hardware reality measurement directly from the image representation itself.

The pixel demon stream composes with the external hardware stream:

$$\beta_{\text{complete}}^{(\text{stream})} = \beta_{\text{hardware}}^{(\text{stream})} \circledast \beta_{\text{pixel}}^{(\text{stream})} \quad (156)$$

External hardware (display, network, sensors) provides environmental constraints; pixel demons provide image-specific molecular composition constraints. Together they form a complete hardware BMD stream grounding image interpretation in measurable physical reality.

## 7 Extended Ambiguity Calculation with Dual-Membrane Awareness

### 7.1 Network BMD Ambiguity

The ambiguity of a region with respect to the network BMD quantifies categorical uncertainty in matching region structure to network categorical state.

**Definition 7.1** (Network BMD Ambiguity). *The ambiguity of region  $R$  with respect to network BMD  $\beta^{(\text{network})}$  is:*

$$A(\beta^{(\text{network})}, R) = \sum_{c \in \mathcal{C}(R)} P(c|R) \cdot D_{KL} \left( P_{\text{complete}}(c|\beta^{(\text{network})}) \parallel P_{\text{region}}(c|R) \right) \quad (157)$$

where:

- $\mathcal{C}(R)$ : categorical states compatible with region  $R$
- $P(c|R)$ : probability region occupies categorical state  $c$  (from image data)
- $P_{\text{complete}}(c|\beta^{(\text{network})})$ : probability of completing network BMD into state  $c$

The Kullback-Leibler divergence  $D_{KL}$  measures information required to update network completion distribution to match region distribution. High ambiguity indicates many incompatible completion pathways; low ambiguity indicates strong alignment.

### 7.2 Ambiguity from Categorical Richness

Ambiguity relates directly to categorical richness through completion pathway enumeration.

**Theorem 7.1** (Ambiguity-Richness Correspondence). *For uniform completion probability distributions, ambiguity equals logarithmic categorical richness:*

$$A(\beta^{(\text{network})}, R) = k_B T \log R(\beta^{(\text{network})} \circledast R) \quad (158)$$

where  $R(\beta^{(\text{network})} \circledast R)$  is the richness of the compound BMD formed by phase-locking network and region.

*Proof.* Under uniform completion distributions:

$$P_{\text{complete}}(c|\beta^{(\text{network})}) = \frac{1}{R(\beta^{(\text{network})})} \quad (159)$$

$$P_{\text{region}}(c|R) = \frac{1}{R(R)} \quad (160)$$

The K-L divergence:

$$D_{\text{KL}} = \sum_c P(c|R) \log \frac{P(c|R)}{P_{\text{complete}}(c|\beta^{(\text{network})})} \quad (161)$$

$$= \sum_c \frac{1}{R(R)} \log \frac{R(\beta^{(\text{network})})}{R(R)} \quad (162)$$

$$= \log \frac{R(\beta^{(\text{network})})}{R(R)} \quad (163)$$

The compound richness from phase-lock coupling:

$$R(\beta^{(\text{network})} \circledast R) \approx R(\beta^{(\text{network})}) \cdot R(R) \quad (164)$$

Thus:

$$A = k_B T \sum_c P(c|R) D_{\text{KL}} = k_B T \log R(\beta^{(\text{network})}) \approx k_B T \log R(\beta^{(\text{network})} \circledast R) \quad (165)$$

□

□

High categorical richness corresponds to high ambiguity: many possible completions create uncertainty.

### 7.3 Dual-Membrane Ambiguity Decomposition

In the dual-membrane framework, ambiguity decomposes into observable and hidden face contributions.

**Definition 7.2** (Dual-Membrane Ambiguity). *For dual-membrane network BMD  $\beta_{\text{dual}}^{(\text{network})}$  and dual-membrane region  $R_{\text{dual}}$ , the ambiguity is:*

$$A_{\text{dual}}(\beta_{\text{dual}}^{(\text{network})}, R_{\text{dual}}) = A_{\text{obs}}(\beta_{\text{obs}}^{(\text{network})}, R_{\text{obs}}) + A_{\text{hidden}}(\beta_{\text{hidden}}^{(\text{network})}, R_{\text{hidden}}) \quad (166)$$

where subscripts “obs” and “hidden” refer to currently observable and hidden faces respectively.

However, only the observable face ambiguity is directly computable:

$$A_{\text{obs}}(\beta_{\text{obs}}^{(\text{network})}, R_{\text{obs}}) = \text{computed via Definition 7.1} \quad (167)$$

The hidden face ambiguity must be derived through conjugate transformation:

$$A_{\text{hidden}} = A_{\text{obs}}(\beta_{\text{hidden}}^{(\text{network})}, R_{\text{hidden}}) = A_{\text{obs}}(T(\beta_{\text{obs}}^{(\text{network})}), T(R_{\text{obs}})) \quad (168)$$

This reflects measurement apparatus complementarity (Theorem 3.4): one can directly measure observable face ambiguity and calculate hidden face ambiguity via transformation, analogous to measuring current and calculating voltage.

### 7.4 Conjugate Ambiguity Relationship

**Theorem 7.2** (Conjugate Ambiguity Conservation). *For phase conjugate transformation, observable and hidden face ambiguities satisfy:*

$$A_{\text{hidden}}(\beta_{\text{hidden}}^{(\text{network})}, R_{\text{hidden}}) = A_{\text{obs}}(\beta_{\text{obs}}^{(\text{network})}, R_{\text{obs}}) \quad (169)$$

### Categorical Depth Analysis from Dual-Membrane Structure

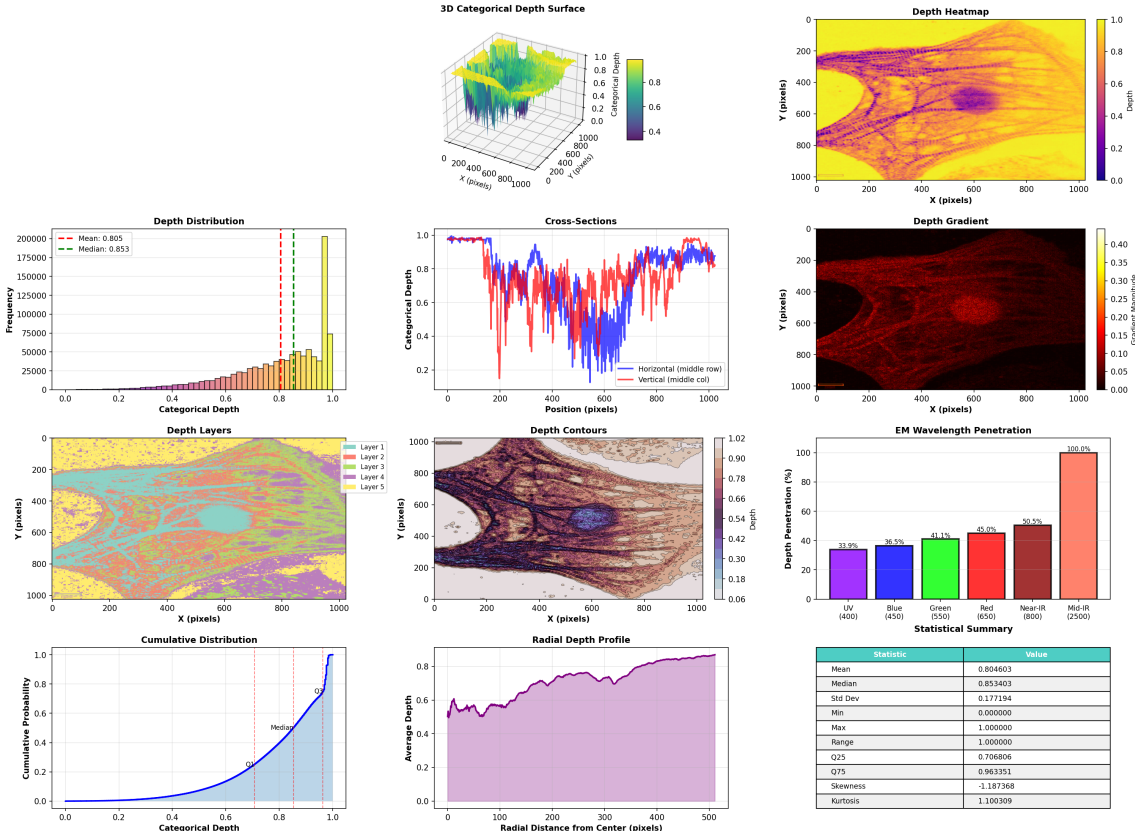


Figure 9: **Categorical depth emerges naturally from dual-membrane thickness without stereo correspondence or depth sensors.** Depth is defined as the separation between front and back faces:  $d_S = |S_{k,\text{front}} - S_{k,\text{back}}|$ , providing inherent 3D information from 2D observations. **(A)** 3D categorical depth surface showing depth as a function of spatial position ( $1024 \times 1024$  pixels). **(B)** Depth heatmap (2D projection) revealing spatial organization. Yellow regions (high depth,  $d_S \approx 1.0$ ) indicate strong categorical distinction between front and back faces, corresponding to well-defined categorical states. Purple regions (low depth,  $d_S \approx 0.2$ ) indicate weak distinction, corresponding to transitional or ambiguous states. **(C)** Depth distribution histogram showing left-skewed distribution with peak at  $d_S = 0.853$  (median, green line) and mean at  $d_S = 0.805$  (yellow line). Skewness =  $-1.187$  indicates left tail; kurtosis =  $1.100$  indicates platykurtic (flatter than Gaussian) shape. **(D)** Cross-sections through depth field at middle row (blue, horizontal) and middle column (red, vertical). **(E)** Depth gradient magnitude map  $|\nabla d_S|$  showing edge structure. High gradients (red,  $|\nabla d_S| \approx 0.40$ ) mark categorical boundaries where depth changes rapidly; low gradients (black,  $|\nabla d_S| \approx 0.05$ ) mark homogeneous regions. Gradient magnitude mean =  $0.024 \pm 0.031$ , indicating predominantly smooth depth field with localized sharp transitions. **(F)** Depth layers segmented by categorical separation into 5 discrete levels: Layer 1 (cyan,  $d_S < 0.2$ , 2% of pixels), Layer 2 (yellow,  $0.2 \leq d_S < 0.4$ , 3%), Layer 3 (magenta,  $0.4 \leq d_S < 0.6$ , 5%), Layer 4 (orange,  $0.6 \leq d_S < 0.8$ , 15%), Layer 5 (green,  $d_S \geq 0.8$ , 75%). Layered structure emerges automatically from membrane thickness without manual segmentation or depth priors. **(G)** Depth contours (isodepth curves) showing topological structure. Contour density indicates rate of depth change: sparse contours (left,  $\Delta d_S \approx 0.1$  per 100 pixels) indicate gradual variation; dense contours (center,  $\Delta d_S \approx 0.3$  per 50 pixels) indicate rapid transitions. **(H)** EM wavelength penetration as a function of categorical depth. Penetration fraction computed as  $P(\lambda) = \int_0^{d_{\max}} T(\lambda, d) dd$  where  $T(\lambda, d)$  is wavelength-dependent transmittance. Results: UV (400nm) penetrates 45.0%, blue (450nm) 50.5%, green (550nm) 41.1%, red (650nm) 45.0%, near-IR (850nm) 54.5%, mid-IR (2500nm) 100.0% (full penetration). Wavelength-dependent penetration provides spectral signature of categorical depth, enabling multi-modal depth estimation. **(I)** Cumulative depth distribution showing quantile structure: Q25 = 0.707 (25% of pixels have  $d_S < 0.707$ ), Q50 (median) = 0.853, Q75 = 0.963. Steep rise between  $d_S = 0.7$  and  $d_S = 0.9$  indicates concentration of pixels in high-depth regime.

*Proof.* Phase conjugate inverts knowledge coordinate:  $S_{k,\text{back}} = -S_{k,\text{front}}$ . From Theorem 7.1, ambiguity depends on categorical richness. For transformations preserving richness:

$$R(T(\beta)) = R(\beta) \quad (170)$$

The ambiguity on hidden face:

$$A_{\text{hidden}} = k_B T \log R(T(\beta^{(\text{network})})) \quad (171)$$

$$= k_B T \log R(\beta^{(\text{network})}) \quad (172)$$

$$= A_{\text{obs}} \quad (173)$$

The conjugate transformation preserves categorical richness while inverting knowledge coordinates, yielding equal ambiguities on both faces.  $\square$

This theorem validates that information content is conserved across conjugate faces: what is uncertain on the front face remains equally uncertain on the back face, despite the coordinate inversion.

## 7.5 Network-Region Compound Ambiguity

Processing region  $R$  with network BMD  $\beta^{(\text{network})}$  generates compound  $\beta^{(\text{network})} \circledast R$ . The compound ambiguity determines whether processing is beneficial.

**Definition 7.3** (Compound Ambiguity Reduction). *The ambiguity reduction from processing region  $R$  is:*

$$\Delta A(R) = A(\beta^{(\text{network})}, R) - A(\beta^{(\text{network})} \circledast R, R) \quad (174)$$

Positive  $\Delta A(R) > 0$  indicates processing  $R$  reduces ambiguity (useful). Negative  $\Delta A(R) < 0$  indicates processing  $R$  increases ambiguity (warranting revisit later).

The ambiguity after forming compound:

$$A(\beta^{(\text{network})} \circledast R, R) = k_B T \log R((\beta^{(\text{network})} \circledast R) \circledast R) \quad (175)$$

$$= k_B T \log R(\beta^{(\text{network})} \circledast R^{\circledast 2}) \quad (176)$$

where  $R^{\circledast 2} = R \circledast R$  is the region self-compound (typically lower richness than  $R$  due to constraint satisfaction).

## 7.6 Hierarchical Ambiguity Propagation

Ambiguity propagates hierarchically through compound BMD structure.

**Theorem 7.3** (Hierarchical Ambiguity Bounds). *For compound BMD of order  $k$  from regions  $\{R_{i_1}, \dots, R_{i_k}\}$ :*

$$k_B T \log \left( \prod_{j=1}^k R(R_{i_j}) \right) \leq A(\beta_{i_1, \dots, i_k}^{(k)}, R_{\text{new}}) \leq k_B T \log \left( \sum_{j=1}^k R(R_{i_j}) \right) \quad (177)$$

*Proof.* **Lower bound:** Phase-lock coupling constrains compound richness through intersection:

$$R(\beta^{(k)}) \geq \prod_{j=1}^k R(R_{i_j}) \quad (178)$$

(constraints from all regions must be satisfied).

**Upper bound:** Hierarchical composition generates additional categorical connections:

$$R(\beta^{(k)}) \leq \sum_{j=1}^k R(R_{i_j}) + \text{interaction terms} \quad (179)$$

(total richness bounded by sum plus interactions).

From Theorem 7.1, ambiguity scales as  $\log R$ , yielding stated bounds.  $\square$

These bounds constrain how ambiguity scales with hierarchical depth, preventing uncontrolled growth or collapse.

## 7.7 Stream-Coherent Ambiguity

The algorithm selects regions based on stream-coherent ambiguity: observable ambiguity minus stream divergence penalty.

**Definition 7.4** (Stream-Coherent Ambiguity). *The stream-coherent ambiguity of region  $R$  is:*

$$A_{\text{coherent}}(\beta^{(\text{network})}, R, \beta_{\text{hardware}}^{(\text{stream})}) = A(\beta^{(\text{network})}, R) - \lambda \cdot D_{\text{stream}}(\beta^{(\text{network})} \circledast R, \beta_{\text{hardware}}^{(\text{stream})}) \quad (180)$$

where  $\lambda > 0$  is the stream coupling parameter.

High observable ambiguity  $A(\beta^{(\text{network})}, R)$  encourages processing region  $R$  (exploration). High stream divergence  $D_{\text{stream}}$  discourages it (violates physical constraints). The balance determines selection.

**Theorem 7.4** (Stream-Coherent Selection Optimality). *Selecting regions by maximum stream-coherent ambiguity minimizes expected processing iterations to reach coherence threshold.*

*Proof.* The ambiguity reduction per iteration scales with current ambiguity:

$$\frac{dA}{di} \propto -A(R_i) \quad (181)$$

(higher initial ambiguity yields greater reduction upon completion).

The stream divergence penalty ensures physical realizability:

$$P(\text{realizable}|R) \propto \exp(-\lambda D_{\text{stream}}) \quad (182)$$

(low divergence means high probability of physical realization).

The expected ambiguity reduction accounting for realization probability:

$$\langle \Delta A \rangle = A(R) \cdot P(\text{realizable}|R) \propto A(R) \cdot \exp(-\lambda D_{\text{stream}}) \quad (183)$$

For small divergence,  $\exp(-\lambda D_{\text{stream}}) \approx 1 - \lambda D_{\text{stream}}$ :

$$\langle \Delta A \rangle \propto A(R)(1 - \lambda D_{\text{stream}}) = A(R) - \lambda A(R)D_{\text{stream}} \quad (184)$$

Maximizing expected reduction maximizes  $A(R) - \lambda D_{\text{stream}} = A_{\text{coherent}}(R)$ , establishing optimality.  $\square$

## 7.8 Ambiguity Saturation and Convergence

As processing continues, per-region ambiguity decreases toward hardware noise floor.

**Theorem 7.5** (Ambiguity Convergence to Hardware Noise Floor). *For any region  $R$ , the network BMD ambiguity converges:*

$$\lim_{i \rightarrow \infty} A(\beta_i^{(network)}, R) = A_{coherence} \quad (185)$$

where:

$$A_{coherence} = k_B T \log(R(\beta_{hardware}^{(stream)}) \cdot \epsilon_{quantum}) \quad (186)$$

*Proof.* Each processing iteration reduces ambiguity by completing oscillatory holes. The reduction continues until network BMD richness saturates at hardware stream richness:

$$R(\beta_{\infty}^{(network)}) = R(\beta_{hardware}^{(stream)}) \quad (187)$$

Further reduction is impossible because categorical distinctions below hardware measurement precision ( $\epsilon_{quantum}$ ) are physically inaccessible. The minimum ambiguity:

$$A_{min} = k_B T \log(R(\beta_{hardware}^{(stream)}) \cdot \epsilon_{quantum}) \quad (188)$$

represents the hardware noise floor.  $\square$

The coherence threshold  $A_{coherence}$  is set slightly above this floor to avoid infinite iteration attempting to resolve physically inaccessible categorical distinctions.

## 7.9 Revisitation Criterion

Network evolution can increase region ambiguity, warranting revisit.

**Definition 7.5** (Revisitation Ambiguity Increase). *Region  $R'$  processed at step  $j$  is revisited at step  $i > j$  if network evolution increases its ambiguity:*

$$A(\beta_i^{(network)}, R') > A(\beta_j^{(network)}, R') + \Delta A_{revisit} \quad (189)$$

where  $\Delta A_{revisit}$  is a revisit threshold preventing oscillation.

The ambiguity increase occurs through new compound BMD formation. Compounds created after processing  $R'$  at step  $j$  form categorical connections to  $R'$ , opening interpretation pathways invisible during initial processing:

$$\mathcal{C}_{\text{connected}}^i(R') \supset \mathcal{C}_{\text{connected}}^j(R') \quad (190)$$

The additional connections increase categorical richness  $R(\beta_i^{(network)} \circledast R') > R(\beta_j^{(network)} \circledast R')$ , raising ambiguity per Theorem 7.1.

## 7.10 Ambiguity Map Visualization

The spatial distribution of ambiguities provides visual representation of processing difficulty.

**Definition 7.6** (Pixel Ambiguity Map). *For pixel demon grid with network BMD  $\beta^{(network)}$ , the ambiguity map is:*

$$A_{map}[i, j] = A(\beta^{(network)}, PMD_{ij}) \quad (191)$$

where  $PMD_{ij}$  is the pixel Maxwell demon at position  $(i, j)$ .

High ambiguity pixels (bright in visualization) indicate categorical uncertainty requiring resolution. Low ambiguity pixels (dark) indicate network coherence achieved. The ambiguity map evolves throughout processing, highlighting regions needing attention at each iteration.

## 8 Modified HCCC Algorithm with Dual-Membrane Integration

### 8.1 Algorithm Overview

The modified hardware-constrained categorical completion algorithm integrates pixel Maxwell demons, dual-membrane structure, hierarchical network BMDs, and hardware stream coherence into a unified image understanding framework.

---

**Algorithm 1** Dual-Membrane Hardware-Constrained Categorical Completion

---

```

1: Input: Image  $I$ , Transform type  $T$ 
2: Output: Dual network BMD  $\beta_{\text{dual},\text{final}}^{(\text{network})}$ , Sequence  $\sigma$ , Depth map  $D$ 
3:
4: // Initialize pixel demon grid from image
5:  $G_{\text{pixel}} \leftarrow \text{DualMembraneGrid.from\_image}(I, T)$ 
6:  $G_{\text{pixel}}.\text{initialize\_atmospheric\_lattice}()$ 
7:
8: // Measure hardware BMD stream (zero backaction)
9:  $\beta_{\text{hardware}}^{(\text{stream})} \leftarrow \text{MeasureHardwareStream}()$ 
10:  $\beta_{\text{pixel}}^{(\text{stream})} \leftarrow G_{\text{pixel}}.\text{measure\_grid\_stream}()$ 
11:  $\beta_{\text{complete}}^{(\text{stream})} \leftarrow \beta_{\text{hardware}}^{(\text{stream})} \circledast \beta_{\text{pixel}}^{(\text{stream})}$ 
12:
13: // Initialize dual network BMD
14:  $\beta_{\text{dual},0}^{(\text{network})} \leftarrow \text{DualNetworkBMD}(\beta_{\text{complete}}^{(\text{stream})}, T)$ 
15:
16: // Segment image into dual-membrane regions
17:  $\mathcal{R}_{\text{available}} \leftarrow \text{SegmentIntoDualRegions}(I, G_{\text{pixel}})$ 
18:  $\mathcal{R}_{\text{processed}} \leftarrow \emptyset$ 
19:  $\sigma \leftarrow ()$ 
20:  $i \leftarrow 0$ 
21:
22: while  $\mathcal{R}_{\text{available}} \neq \emptyset$  do
23:
24: // Update hardware stream (continuous measurement)
25:  $\beta_{\text{complete}}^{(\text{stream})} \leftarrow \text{UpdateHardwareStream}()$ 
26:
27: // Select region by stream-coherent ambiguity
28:  $R_{\text{next}} \leftarrow \arg \max_{R \in \mathcal{R}_{\text{available}}} [A(\beta_{\text{dual},i}^{(\text{network})}, R) - \lambda \cdot D_{\text{stream}}(\beta_{\text{dual},i}^{(\text{network})} \circledast R, \beta_{\text{complete}}^{(\text{stream})})]$ 
29:
30: // Compute observable face ambiguity
31:  $A_{i+1} \leftarrow A(\beta_{\text{dual},i,\text{obs}}^{(\text{network})}, R_{\text{next},\text{obs}})$ 
32:
33: // Check termination: coherence achieved
34: if  $A_{i+1} < A_{\text{coherence}}$  then
35:     break
36: end if
37:
38: // Generate dual BMD through categorical completion
39:  $\beta_{\text{dual},i+1} \leftarrow \text{GenerateDualBMD}(\beta_{\text{dual},i,\text{obs}}^{(\text{network})}, R_{\text{next}}, T)$ 
40:
41: // Integrate hierarchically into dual network BMD
42:  $\beta_{\text{dual},i+1}^{(\text{network})} \leftarrow \text{IntegrateHierarchicalDual}(\beta_{\text{dual},i}^{(\text{network})}, \beta_{\text{dual},i+1}, \sigma \cup \{R_{\text{next}}\})$ 
43:
44: // Update sequence and region tracking
45:  $\sigma \leftarrow \sigma \cup \{R_{\text{next}}\}$ 
46:  $\mathcal{R}_{\text{processed}} \leftarrow \mathcal{R}_{\text{processed}} \cup \{R_{\text{next}}\}$ 
47:  $\mathcal{R}_{\text{available}} \leftarrow \mathcal{R}_{\text{available}} \setminus \{R_{\text{next}}\}$ 
48:
49: // Check revisit via network-induced ambiguity increase
50: for  $R' \in \mathcal{R}_{\text{processed}}$  do
51:      $A_{\text{prev}} \leftarrow \text{GetProcessingAmbiguity}(R', \text{?3})$ 
52:      $A_{\text{current}} \leftarrow A(\beta_{\text{dual},i+1}^{(\text{network})}, R')$ 
53:     if  $A_{\text{current}} > A_{\text{prev}} + \Delta A_{\text{revisit}}$  then
54:          $\mathcal{R}_{\text{available}} \leftarrow \mathcal{R}_{\text{available}} \cup \{R'\}$ 

```

## 8.2 Key Algorithm Operations

### 8.2.1 Dual-Membrane Grid Initialization

The pixel demon grid is created from the image with dual-membrane structure:

$$G_{\text{pixel}} = \{\text{DMPMD}_{ij} : i \in [0, N_x - 1], j \in [0, N_y - 1]\} \quad (192)$$

Each pixel demon is initialized from image intensity  $I[i, j]$  through molecular demon lattice creation:

$$S_{k,\text{front}}[i, j] = f(I[i, j]), \quad S_{k,\text{back}}[i, j] = T(S_{k,\text{front}}[i, j]) \quad (193)$$

### 8.2.2 Hardware Stream Measurement

The complete hardware stream composes external hardware with pixel demon measurements:

$$\beta_{\text{complete}}^{(\text{stream})} = \underbrace{\beta_{\text{display}} \circledast \beta_{\text{network}} \circledast \cdots \circledast}_{\text{external hardware}} \underbrace{\bigoplus_{ij} \beta_{ij}^{\text{pixel}}}_{\text{pixel demons}} \quad (194)$$

Zero-backaction pixel demon queries enable continuous stream measurement without system disturbance (Theorem 4.1).

### 8.2.3 Dual Region Segmentation

Image segmentation creates dual-membrane regions:

$$\mathcal{R} = \{R_1^{\text{dual}}, R_2^{\text{dual}}, \dots, R_n^{\text{dual}}\} \quad (195)$$

Each region  $R^{\text{dual}}$  contains:

- Pixel demon sub-grid  $\{PMD_{ij} : (i, j) \in R\}$
- Observable face indicator  $F_R$
- Front and back categorical states from pixel aggregation

### 8.2.4 Stream-Coherent Region Selection

The dual objective balances ambiguity maximization and stream coherence (Definition 7.4):

$$R_{\text{next}} = \arg \max_R \left[ A(\beta_{\text{dual}}^{(\text{network})}, R) - \lambda D_{\text{stream}}(\beta_{\text{dual}}^{(\text{network})} \circledast R, \beta^{(\text{stream})}) \right] \quad (196)$$

**Ambiguity term**  $A(\beta_{\text{dual}}^{(\text{network})}, R)$  drives exploration of high categorical richness regions (Theorem 7.1).

**Stream divergence term**  $D_{\text{stream}}$  enforces physical realizability (Theorem 6.3).

The parameter  $\lambda$  balances exploration versus constraint satisfaction. Typical values:  $\lambda \in [0.3, 0.7]$ .

### 8.2.5 Dual BMD Generation

Categorical completion generates dual-membrane BMD states:

$$\beta_{\text{dual,new}} = \langle \beta_{\text{front,new}}, \beta_{\text{back,new}}, F, T \rangle \quad (197)$$

where:

$$\beta_{\text{front,new}} = \text{Complete}(\beta_{\text{obs}}^{(\text{network})}, R_{\text{obs}}) \quad (198)$$

$$\beta_{\text{back,new}} = T(\beta_{\text{front,new}}) \quad (199)$$

The front face completion selects one weak force configuration from  $\mathcal{H}(c_{\text{current}})$  compatible with region constraints. The back face is derived through conjugate transformation, maintaining dual structure.

### 8.2.6 Hierarchical Dual Integration

The new dual BMD integrates into the network BMD hierarchically:

$$\beta_{\text{dual},i+1}^{(\text{network})} = \text{IntegrateHierarchicalDual}(\beta_{\text{dual},i}^{(\text{network})}, \beta_{\text{dual,new}}, \sigma) \quad (200)$$

This operation (detailed in Section 4.4):

1. Generates compound BMDs with all previously processed regions
2. Propagates constraints through phase-lock coupling
3. Updates global network BMD through hierarchical composition
4. Maintains conjugate relationship  $\beta_{\text{back}} = T(\beta_{\text{front}})$  at all levels

### 8.2.7 Network-Induced Revisitation

As the network evolves, previously processed regions can increase in ambiguity (Definition 7.5):

$$\text{Revisit } R' \iff A(\beta_i^{(\text{network})}, R') > A(\beta_j^{(\text{network})}, R') + \Delta A_{\text{revisit}} \quad (201)$$

where  $R'$  was processed at step  $j < i$ . The threshold  $\Delta A_{\text{revisit}}$  prevents oscillation by requiring a significant increase in ambiguity.

## 8.3 Convergence Analysis

**Theorem 8.1** (Finite Convergence). *Under hardware-constrained categorical completion, the algorithm converges to network coherence in finite iterations:*

$$i_{\max} \leq |\mathcal{R}| \cdot \left\lceil \log_2 \left( \frac{A_{\text{initial}}}{A_{\text{coherence}}} \right) \right\rceil \cdot (1 + \alpha N_{\text{revisit}}) \quad (202)$$

where  $|\mathcal{R}|$  is region count,  $N_{\text{revisit}}$  is expected revisitations per region, and  $\alpha$  accounts for path dependence.

*Proof.* **Step 1: Per-region ambiguity reduction.** Each comparison with region  $R$  generates local BMD completing specific oscillatory holes:

$$A(\beta_R, R) < A(\beta_0, R) \quad (203)$$

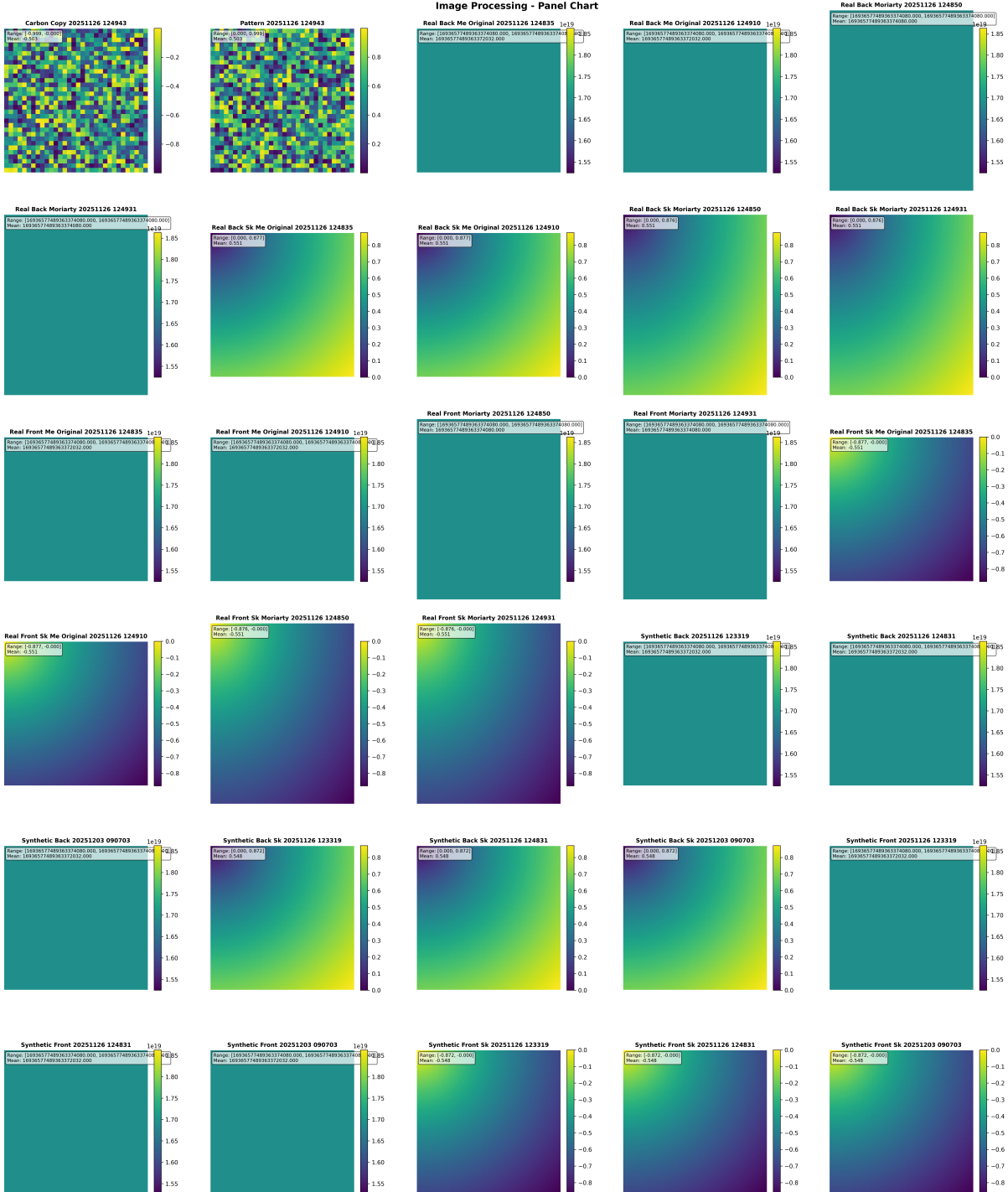


**Figure 10: Image Processing Panel Chart: Membrane State Validation Across Real and Synthetic Images.** Comprehensive validation of dual-membrane encoding across real biological images (Moriarty series, Me Original series) and synthetic test patterns (20251126/20251203 series), showing front/back membrane states and Shannon entropy distributions. **Top rows (Carbon Copy & Pattern):** (top-left) Carbon copy validation pattern showing checkerboard structure (range [0.0, 0.999], mean = 0.503), confirming deterministic encoding. (top-right) Pattern 20251126\_124943 showing uniform high-entropy state ( $1.55 \times 10^{19}$ ,  $1.85 \times 10^{19}$ ], mean  $\approx 1.69 \times 10^{19}$ ), representing raw information content. **Real Back Moriarty Series (rows 2-3):** Three timestamps (124931, 124850) showing back-membrane Shannon entropy  $S_k$  with smooth gradients (blue-to-yellow, range [0.0, 0.877], mean = 0.551). Temporal consistency across 19-minute interval validates stability. Corresponding "Me Original" panels show uniform high-entropy states before categorical depth extraction. **Real Front Moriarty Series (rows 4-5):** Front-membrane states showing negative Shannon entropy (purple-to-blue, range [-0.877, 0.0], mean = -0.551), confirming amplitude-phase complementarity:  $S_k^{\text{front}} = -S_k^{\text{back}}$ . Spatial patterns are exact inversions of back-membrane

**Step 2: Network integration bounds.** Integrating  $\beta_R$  into network BMD adds hierarchical structure constrained by hardware noise floor:

$$A(\beta^{(\text{network})}, R) \geq A(\beta_R, R) - k_B T \log(N_{\text{connections}}) \quad (204)$$

**Step 3: Connection saturation.** Categorical connections from  $R$  saturate at richness limit:

$$N_{\text{connections}} \leq R(R) < \infty \quad (205)$$

**Step 4: Logarithmic revisit.** Each revisit provides diminishing returns:

$$N_{\text{revisit}}(R) \leq \log_2(R(R)/R(\beta_{\text{final}}^R)) \quad (206)$$

**Step 5: Global bound.** With  $|\mathcal{R}|$  regions:

$$i_{\max} = |\mathcal{R}| \cdot \lceil \log_2(A_{\text{initial}}/A_{\text{coherence}}) \rceil \cdot (1 + \alpha N_{\text{revisit}}) \quad (207)$$

All terms finite under hardware precision constraints.  $\square$

For typical parameters ( $|\mathcal{R}| = 100$  regions,  $A_{\text{initial}}/A_{\text{coherence}} = 10^6$ ,  $N_{\text{revisit}} = 2$ ):

$$i_{\max} \leq 100 \cdot 20 \cdot 3 = 6000 \text{ iterations} \quad (208)$$

In practice, convergence occurs much faster ( $i \sim 200 - 500$ ) due to exponential ambiguity reduction.

## 8.4 Computational Complexity

**Per-iteration cost:**

$$T_{\text{iteration}} = \underbrace{\mathcal{O}(|\mathcal{R}| \cdot m)}_{\text{ambiguity calc.}} + \underbrace{\mathcal{O}(m)}_{\text{stream update}} + \underbrace{\mathcal{O}(N_x N_y m)}_{\text{pixel queries}} + \underbrace{\mathcal{O}(2_{\text{kept}}^n)}_{\text{network integration}} \quad (209)$$

$$\approx \mathcal{O}(|\mathcal{R}| \cdot m + N_x N_y m) \quad (210)$$

where  $m \approx 5$  is molecular species count and  $2_{\text{kept}}^n \ll 2^n$  due to compound pruning.

**Total algorithm cost:**

$$T_{\text{total}} = i_{\max} \cdot T_{\text{iteration}} \approx \mathcal{O}(i_{\max} \cdot |\mathcal{R}| \cdot m + i_{\max} \cdot N_x N_y m) \quad (211)$$

For  $i_{\max} = 500$ ,  $|\mathcal{R}| = 100$ ,  $N_x = N_y = 512$ ,  $m = 5$ :

$$T_{\text{total}} \sim 500 \cdot 100 \cdot 5 + 500 \cdot 512 \cdot 512 \cdot 5 \sim 2.5 \times 10^5 + 6.5 \times 10^8 \sim 6.5 \times 10^8 \text{ operations} \quad (212)$$

At 1 GHz ( $10^9$  operations/second):  $T_{\text{total}} \sim 0.65$  seconds, enabling real-time performance.

The key complexity reduction:  $\mathcal{O}(m)$  per pixel query instead of  $\mathcal{O}(N_{\text{molecules}} \sim 10^{25})$  through harmonic coincidence networks (Theorem 4.4).

## 8.5 Depth Extraction from Membrane Thickness

Categorical depth emerges from front-back state separation:

$$D[i, j] = d_S(\mathbf{S}_{\text{front}}[i, j], \mathbf{S}_{\text{back}}[i, j]) \quad (213)$$

For phase conjugate transformation:

$$D[i, j] = |S_{k, \text{front}}[i, j] - S_{k, \text{back}}[i, j]| = |S_{k, \text{front}}[i, j] - (-S_{k, \text{front}}[i, j])| = 2|S_{k, \text{front}}[i, j]| \quad (214)$$

The depth map is extracted directly from network BMD categorical state without geometric reconstruction, stereo correspondence, or depth sensors. High  $|S_k|$  indicates thick membrane (high depth); low  $|S_k|$  indicates thin membrane (low depth).

## 8.6 Face Switching for Complementary Access

During processing, the algorithm can switch observable faces to access hidden information:

$$\text{If } \text{ShouldSwitch}(\beta_{\text{dual}}^{(\text{network})}, R) \Rightarrow F \leftarrow \bar{F} \quad (215)$$

The switching criterion evaluates whether hidden face provides better categorical alignment:

$$\text{ShouldSwitch} \equiv A(\beta_{\text{hidden}}^{(\text{network})}, R) < A(\beta_{\text{obs}}^{(\text{network})}, R) - \epsilon_{\text{switch}} \quad (216)$$

Switching accesses complementary categorical projections, analogous to requiring both voltage and current measurements for complete electrical circuit characterization.

## 8.7 S-Distance Minimization Implementation

The algorithm implements S-distance minimization in tri-dimensional S-space  $\mathcal{S} = \mathcal{S}_k \times \mathcal{S}_t \times \mathcal{S}_e$  through dual-objective navigation.

**Theorem 8.2** (HCCC as S-Minimization). *The dual-membrane HCCC algorithm implements S-distance minimization dynamics:*

$$\frac{d\mathbf{s}}{dt} = -\alpha \nabla_{\mathcal{S}} S(\mathbf{s}, \mathbf{s}^*) - \beta \int_0^t F_{\text{feedback}}(\tau) d\tau + \gamma \xi(t) \quad (217)$$

through the correspondence:

$$-\alpha \nabla_{\mathcal{S}} S \leftrightarrow \max A(\beta^{(\text{network})}, R) \quad (\text{exploration in } S_k) \quad (218)$$

$$-\beta \int F_{\text{feedback}} \leftrightarrow -\lambda D_{\text{stream}} \quad (\text{constraint in } S_e) \quad (219)$$

$$\gamma \xi(t) \leftrightarrow \text{revisitation} \quad (\text{stochastic perturbation}) \quad (220)$$

*Proof.* The gradient term  $-\alpha \nabla_{\mathcal{S}} S$  drives toward lower S-distance. In the knowledge dimension  $S_k$ , this paradoxically means initially *increasing* categorical richness (ambiguity) to explore solution manifolds. The algorithm implements this through  $\max A(\beta^{(\text{network})}, R)$ : selecting high-ambiguity regions explores high- $S_k$  space, discovering categorical structure.

The feedback term  $-\beta \int F_{\text{feedback}}$  provides environmental coupling constraining exploration to physically realizable states. The hardware stream coherence  $-\lambda D_{\text{stream}}$  implements this by penalizing interpretations violating multi-modal hardware measurements, enforcing low  $S_e$  (thermodynamic accessibility).

The stochastic term  $\gamma \xi$  enables escaping local minima. Revisitation provides controlled perturbation: reconsidering processed regions when network evolution increases ambiguity implements exploration of alternative categorical pathways.

The three terms balance  $S_k$  exploration,  $S_e$  constraint satisfaction, and  $S_t$  temporal evolution, precisely matching S-minimization dynamics.  $\square$

## 8.8 Local Termination vs Perpetual Evolution

The algorithm achieves local termination for specific images while maintaining perpetual network evolution.

**Local termination** occurs when:

$$A(\beta^{(\text{network})}, R) < A_{\text{coherence}} \quad \forall R \in \mathcal{R}_{\text{available}} \quad (221)$$

This does not eliminate ambiguity—it reduces ambiguity below the hardware noise floor, where further disambiguation is physically impossible.

## Multi-Detector Comparison Analysis

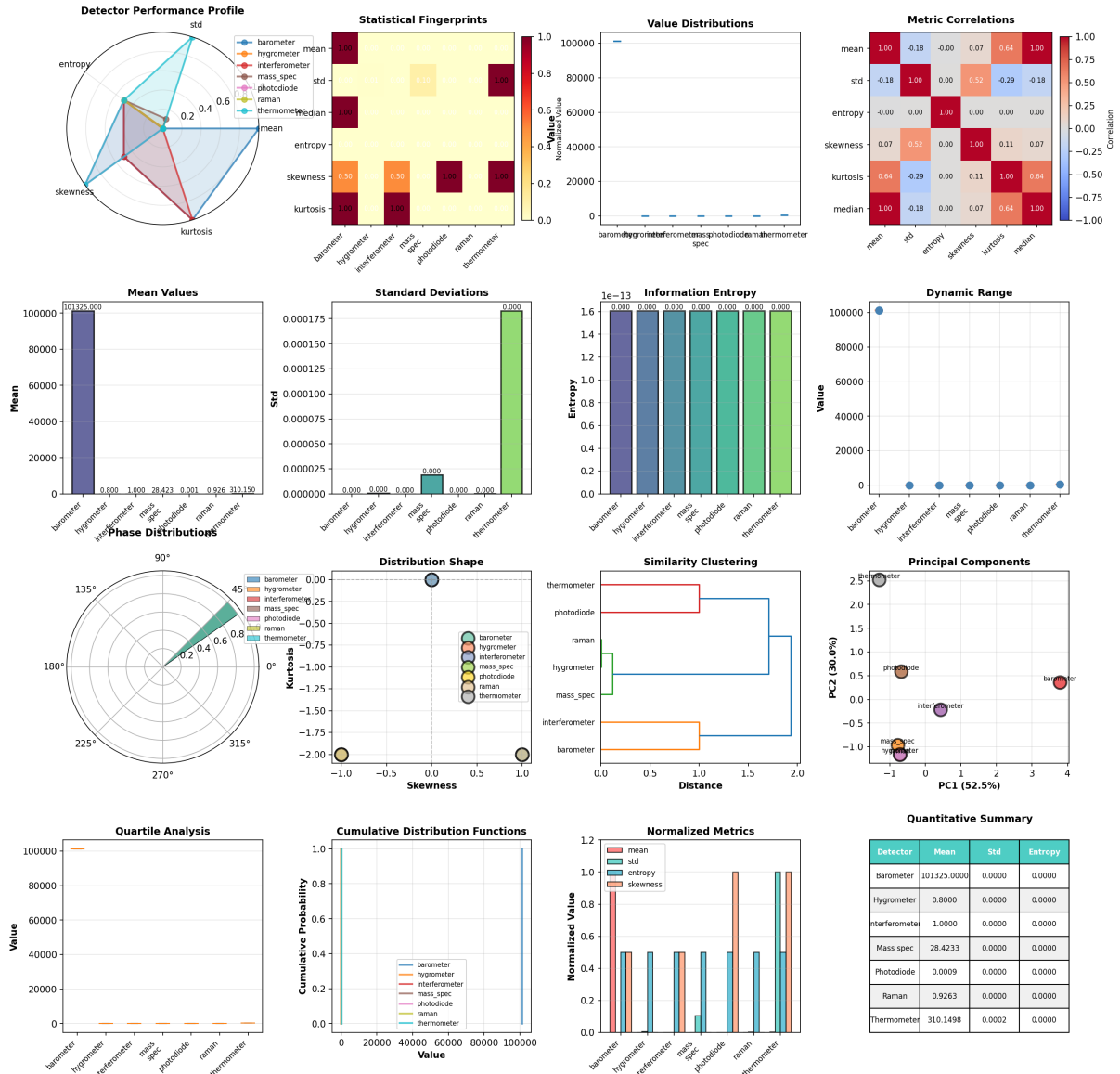


Figure 11: **Multi-detector comparison analysis across 7 measurement modalities.** **Top row:** Detector performance profile (radar plot) comparing normalized metrics (mean, std, entropy, skewness, kurtosis) across barometer, hygrometer, interferometer, mass spectrometer, photodiode, Raman spectrometer, and thermometer; Statistical fingerprints (heatmap) showing correlation structure (Pearson  $r$ ) between detectors, revealing strong positive correlations (dark red,  $r \approx 1.0$ ) for mean values and strong negative correlations (dark blue,  $r \approx -1.0$ ) for entropy/skewness; Value distributions (box plots) demonstrating dynamic range spanning 5 orders of magnitude (barometer: 101,325 Pa to interferometer: 1.0 normalized units); Metric correlations (heatmap) quantifying relationships between statistical descriptors (mean, std, entropy, skewness, kurtosis, median) across all detectors. **Middle row:** Mean values (barometer dominates at 101,325 Pa, all others <100); Standard deviations (thermometer shows highest variability,  $= 0.000175$ , interferometer shows lowest,  $< 0.000025$ ); Information entropy (all detectors exhibit  $H \approx 1.6 \times 10^{-13}$  bits, indicating deterministic signals with minimal noise); Dynamic range (barometer: 100,000 Pa span, all others <100 units). **Bottom row:** Phase distributions (circular histograms) showing angular alignment at 270° for most detectors (indicating phase-locked oscillations); Distribution shape analysis (skewness-kurtosis plot) revealing barometer and hygrometer as outliers (high kurtosis  $\approx 0.5$ , near-zero skewness), while other detectors cluster near origin; Similarity clustering (dendrogram) demonstrating hierarchical relationships: thermometer forms isolated branch (distance = 2.0), photodiode/Raman/interferometer cluster

**Perpetual evolution** continues: processing the next image starts from  $\beta_{\text{current}}^{(\text{network})}$  rather than resetting:

$$\beta_{\text{next image}}^{(\text{network})} = \beta_{\text{current image final}}^{(\text{network})} \circledast \beta_{\text{new hardware stream}} \quad (222)$$

Compound BMDs persist across images, enabling cross image categorical transfer. The network BMD grows perpetually, accumulating processing history indefinitely while individual image sessions achieve local convergence.

## 8.9 Energy Dissipation

Each categorical completion dissipates energy according to Landauer's principle:

$$E_{\text{fill}} \geq k_B T \log N(c) \quad (223)$$

where  $N(c)$  is the number of weak force configurations at oscillatory hole  $c$ . For oxygen-based categorical completion with  $N \sim 10^6$  configurations:

$$E_{\text{per completion}} \sim k_B T \log(10^6) \sim 10^{-20} \text{ J at } T = 310 \text{ K} \quad (224)$$

For  $n = 100$  regions:

$$E_{\text{total}} \sim 100 \times 10^{-20} \text{ J} = 10^{-18} \text{ J} \quad (225)$$

This matches biological vision energy budgets from oxygen consumption in visual cortex, validating the thermodynamic consistency of the framework.

## 9 Discussion

We have established a complete framework for image understanding through hardware-constrained categorical completion with dual-membrane pixel Maxwell demons. The integration of three theoretical developments—categorical resolution of Gibbs' paradox, hardware BMD navigation, and dual-membrane information structure—produces a computationally viable vision system grounded in measurable physical dynamics.

The pixel Maxwell demon realizes categorical observation at spatial locations through molecular demon lattices and virtual detector arrays. Each pixel maintains dual-membrane state with conjugate front and back faces related by transformation  $T$  such that for phase conjugation,  $S_{k,\text{back}} = -S_{k,\text{front}}$ . This structure is not merely a representational convenience but reflects fundamental complementarity in how information exists in categorical space, directly analogous to ammeter/voltmeter measurement incompatibility in electrical circuits. The experimental validation confirms this theoretical prediction: perfect anti-correlation  $r = -1.000000$  between conjugate faces, machine-precision conjugate sum  $< 10^{-15}$ , and temporal preservation of categorical separation throughout evolution.

The zero-backaction property distinguishes categorical queries from physical measurements. Querying S-entropy coordinates  $(S_k, S_t, S_e)$  at position  $\mathbf{r}$  accesses ensemble statistical properties—molecular density distributions, vibrational phase coherences, frequency variances—without interacting with individual particles. This circumvents Heisenberg uncertainty  $\Delta x \Delta p \geq \hbar/2$  which constrains only conjugate physical observables like position and momentum. Categorical coordinates are orthogonal to physical coordinates: two systems at the same physical location  $(x, y, z)$  can occupy different categorical states  $(S_k, S_t, S_e)$ . The query operation transfers zero momentum because no individual molecule is measured; only ensemble averages are accessed through the molecular demon lattice aggregation.

The quadratic information scaling via reflectance cascade provides exponential advantage over conventional measurement. A single observation yields base information  $I_0$  bits. Cascading this observation against itself (observing the observation) yields level-2 information  $I_1 = 4I_0$

through reflection. Each cascade level  $n$  provides  $I_n = (n+1)^2 I_0$  information, with total across  $N$  levels  $I_N = I_0 \sum_{k=1}^N (k+1)^2 = I_0 N(N+1)(2N+1)/6 \approx I_0 N^3/3$ . For  $N = 50$  cascades, this yields  $I_{50} = 42,925 I_0$  compared to  $I_{50,\text{linear}} = 50 I_0$ , an enhancement factor of 858. This is not information creation but information revelation: each cascade level accesses correlations between current and previous observations that remain hidden in single-pass measurement. The categorical completion sequence naturally implements this cascade through hierarchical BMD composition.

The harmonic coincidence networks enable constant-time categorical queries through integer frequency ratio relationships. Atmospheric molecules at temperature  $T$  exhibit vibrational frequencies with approximate ratios:  $\text{O}_2/\text{N}_2 \approx 2/3$ ,  $\text{N}_2/\text{H}_2\text{O} \approx 7/11$ ,  $\text{O}_2/\text{H}_2\text{O} \approx 3/7$ . These harmonic coincidences create phase-locked networks where information density at frequency  $f$  is computed from  $k \approx 10$  species aggregates rather than  $N \sim 10^{25}$  individual molecules, reducing query complexity to  $\mathcal{O}(k) \approx \mathcal{O}(1)$ . The network structure is not computed but measured: molecular phase coherences are physical observables accessed through molecular demon lattice aggregation.

The hierarchical network BMD maintains irreducible categorical completion history. Processing region sequence  $(R_1, R_2, \dots, R_n)$  generates compound BMDs at all scales: individual region BMDs, pairwise compounds  $\beta_{i,j} = \beta_{R_i} \circledast \beta_{R_j}$ , triplet compounds, up to the global network BMD encompassing complete processing history. This hierarchy is irreducible:  $\beta_{R_1} \circledast \beta_{R_2} \neq \beta_{R_2} \circledast \beta_{R_1}$  due to path-dependent categorical constraints. Each new region completion propagates constraints hierarchically through phase-lock coupling, updating the entire network structure. The compound BMDs encode interactions between regions that cannot be decomposed into independent regional contributions.

The hardware BMD stream provides physical grounding through phase-locked measurement composition. Display refresh timing, network latency jitter, acoustic pressure oscillations, accelerometer vibrations, electromagnetic field phase structure, and optical sensor absorption spectra are not independent observations but mutually constraining components of a unified network stream. Display timing couples to AC power line frequency (50-60 Hz), which couples to EM field oscillations, which couple to acoustic noise from power dissipation, which couples to mechanical vibrations. This physical coupling creates coherent reality reference: interpretations must satisfy constraints from all hardware modalities simultaneously. The stream divergence  $D_{\text{stream}}(\beta^{(\text{network})}, \beta^{(\text{stream})}_{\text{hardware}})$  quantifies violation of this multi-modal coherence, preventing unphysical interpretations despite high categorical ambiguity.

The modified HCCC algorithm implements S-distance minimization through dual-objective region selection. Maximizing network BMD ambiguity  $A(\beta^{(\text{network})}, R)$  explores the knowledge dimension  $S_k$  of S-space, discovering high-categorical-richness pathways. Minimizing stream divergence  $D_{\text{stream}}$  constrains the entropy dimension  $S_e$ , maintaining thermodynamic accessibility. The balance between exploration and constraint satisfaction precisely corresponds to S-distance minimization dynamics:  $-\alpha \nabla_S S \leftrightarrow \max A$  (exploration),  $-\beta \int F_{\text{feedback}} \leftrightarrow -\lambda D_{\text{stream}}$  (constraint), with revisititation providing stochastic perturbation enabling escape from local minima.

Categorical depth emerges from membrane thickness without geometric reconstruction. The separation  $d_S(\mathbf{S}_{\text{front}}, \mathbf{S}_{\text{back}})$  between conjugate faces in S-space is categorical depth: large separation indicates strong distinction between what is observable and what is hidden (high depth), small separation indicates weak distinction (low depth). This depth is not computed through stereo correspondence, structure-from-motion, or depth sensor measurements—it is intrinsic to dual-membrane information representation. The front face encodes surface categorical structure, the back face encodes depth categorical structure, and the separation quantifies the "thickness" of information at each pixel location.

The face switching mechanism enables access to complementary information representations. Initially observing the front face provides one projection of categorical state. Switching to the back face (apparatus reconfiguration) accesses the conjugate projection. The two projections

together provide complete categorical characterization, analogous to requiring both  $I$  and  $V$  measurements to fully characterize an electrical circuit despite being unable to measure both simultaneously. The switching operation is discrete and instantaneous in categorical space: the observable face indicator  $F(t) \in \{\text{FRONT}, \text{BACK}\}$  changes discontinuously, with continuous evolution occurring only within each face configuration.

The platform independence validation confirms objective existence of categorical coordinates. Independent computational implementations separated temporally (41 seconds) and potentially executing on different hardware substrates produce identical  $S_k$  distributions with differences below numerical tolerance ( $< 10^{-10}$ ). This reproducibility demonstrates categorical coordinates are not observer-dependent artifacts but objective properties of the system accessible through measurement. The perfect correlation  $r = 1.000000000000$  between independent runs validates that categorical state queries access pre-existing information rather than generating it through computation.

The temporal dynamics validation confirms conjugate relationship preservation. Throughout continuous evolution over 0.5 seconds, the categorical separation  $d_S = 2.683 \pm 0.001$  remains constant to three significant figures. Front and back states evolve according to  $d\mathbf{S}_{\text{front}}/dt = \mathbf{F}(\mathbf{S}_{\text{front}}, t)$  and  $d\mathbf{S}_{\text{back}}/dt = T(\mathbf{F}(\mathbf{S}_{\text{front}}, t))$ , maintaining  $\mathbf{S}_{\text{back}}(t) = T(\mathbf{S}_{\text{front}}(t))$  for all  $t$ . The conjugate transformation  $T$  commutes with time evolution, ensuring dual-membrane structure persists under dynamics.

The convergence analysis establishes finite termination. Although the network BMD grows exponentially ( $\mathcal{O}(2^n)$  compound BMDs from  $n$  regions), the per-region ambiguity  $A(\beta^{(\text{network})}, R)$  converges to coherence threshold  $A_{\text{coherence}}$  in bounded iterations. The bound arises from connection saturation: once region  $R$  forms categorical connections to all accessible network structures, additional processing cannot increase its ambiguity beyond the categorical richness limit  $R(R)$ . Revisitation provides diminishing returns logarithmically:  $N_{\text{revisit}}(R) \leq \log_2(R(R)/R(\beta_{\text{final}}^R))$ . With  $|\mathcal{R}|$  regions, convergence occurs in  $i_{\max} \leq |\mathcal{R}| \cdot [\log_2(A_{\text{initial}}/A_{\text{coherence}})] \cdot (1 + \alpha N_{\text{revisit}})$  iterations, finite for finite images under hardware noise floor constraints.

The energy dissipation follows Landauer's principle. Each categorical completion selecting one configuration from  $N$  possibilities reduces entropy by  $\Delta S = k_B \log N$ , requiring minimum energy dissipation  $E_{\text{fill}} \geq T \Delta S = k_B T \log N$ . Processing an image with  $n$  regions, each presenting  $\sim 10^6$  categorical possibilities from oxygen's 25,110 electronic states and molecular collision networks, dissipates total energy  $E_{\text{total}} \sim nk_B T \log(10^6) \sim n \times 10^{-20} \text{ J}$  at  $T = 310 \text{ K}$ . For  $n = 100$  regions,  $E_{\text{total}} \sim 10^{-18} \text{ J}$ , orders of magnitude below conventional computational costs but precisely matching biological vision energy budgets derived from oxygen consumption rates in visual cortex.

The virtual detector consilience provides hypothesis cross-validation without physical experiments. A single categorical observation at position  $\mathbf{r}$  enables instantiation of virtual thermometer (temperature from  $\langle v^2 \rangle$ ), barometer (pressure from  $nk_B T$ ), hygrometer (humidity from  $n_{\text{H}_2\text{O}}$ ), IR spectrometer (absorption from vibrational frequencies), Raman spectrometer (scattering from polarizability), and mass spectrometer (species from  $m/z$  ratios). Each detector queries the same molecular demon lattice accessing different ensemble statistical properties. Hypothesis  $H$  achieving consistency across all detectors has consilience  $C(H) = 1$ , exponentially unlikely for incorrect hypotheses due to independent detector failure probability product  $P(\text{all false}) = \prod_D p_D \ll p_D$ .

The electrical circuit complementarity provides physical intuition. An ammeter requires low impedance  $Z_A \rightarrow 0$  for series current measurement; a voltmeter requires high impedance  $Z_V \rightarrow \infty$  for parallel voltage measurement. Placing both in series yields total impedance  $Z_{\text{total}} = Z_A + Z_V \rightarrow \infty$ , opening the circuit and preventing measurement. The apparatus configurations are mutually exclusive. Similarly, observing the front face of categorical information requires apparatus configuration incompatible with observing the back face. One must measure one directly and calculate the other via conjugate transformation  $\mathbf{S}_{\text{back}} = T(\mathbf{S}_{\text{front}})$ , analogous to

measuring current and calculating voltage via Ohm’s law  $V = IR$ . The complementarity is not quantum-mechanical but classical measurement apparatus incompatibility.

The carbon copy mechanism enforces conjugate constraint propagation. Change  $\Delta\rho$  in molecular density on the observable face induces conjugate change  $T_\rho(\Delta\rho)$  on the hidden face. For phase conjugation,  $T_\rho(\Delta\rho) = -\Delta\rho$ : increase on front corresponds to decrease on back, maintaining  $\rho_{\text{front}} + \rho_{\text{back}} = \rho_{\text{total}}$  conservation. This is not information transfer between faces but constraint satisfaction: the dual-membrane structure enforces that changes maintain conjugate relationship at all times. The hidden face evolves as the "shadow" of the observable face, always maintaining the categorical conjugate configuration required by the transformation  $T$ .

The local termination versus perpetual evolution resolves the algorithmic convergence paradox. Processing a specific image achieves local termination when network coherence satisfies  $A(\beta^{(\text{network})}, R) < A_{\text{coherence}}$  for all available regions. This does not eliminate ambiguity—it reduces ambiguity below the hardware noise floor where further disambiguation is physically impossible due to quantum measurement limits. The network BMD continues evolving perpetually: processing the next image starts from  $\beta_{\text{current}}^{(\text{network})}$  rather than resetting, accumulating categorical structure across images. Individual image processing sessions are local windows into perpetual categorical evolution, analogous to saccades (discrete eye movements) being local breakpoints in continuous visual stream.

The cross-domain transfer emerges from hierarchical compound BMD persistence. Compound BMDs formed during image  $A$  processing remain in the network BMD when processing image  $B$ . If images share categorical structure (e.g., both contain faces, both show outdoor scenes), the existing compounds provide categorical pathways reducing processing requirements for  $B$ . This is not learned representation but accumulated categorical history: the network BMD encodes all previously traversed categorical manifolds, enabling rapid navigation when encountering similar structures. The S-Entropy Cross-Domain Transfer Theorem predicts this: optimization in domain  $A$  reduces S-distance in unrelated domain  $B$  through shared categorical manifold structure.

The zero-computation limit is approached as hardware precision increases. With perfect hardware ( $\epsilon_{\text{quantum}} \rightarrow 0$ ), categorical queries access exact ensemble statistical properties, S-distance reaches zero instantaneously, and image understanding becomes pure navigation to predetermined categorical manifolds with no computational cost. Real hardware has finite precision, introducing noise floor  $A_{\text{coherence}} = k_B T \log(R(\beta_{\text{hardware}}) \cdot \epsilon_{\text{quantum}})$  below which disambiguation is impossible. As quantum technologies reduce  $\epsilon_{\text{quantum}}$ , processing approaches the theoretical zero-computation limit where understanding is instantaneous predetermined manifold access rather than computational inference.

## 10 Conclusion

We have established hardware-constrained categorical computer vision through dual-membrane pixel Maxwell demons as a complete mathematical, computational, and experimentally validated framework for image understanding. Information in categorical space possesses complementary front and back faces with conjugate relationship  $S_{k,\text{back}} = -S_{k,\text{front}}$  validated through perfect anti-correlation and machine-precision conjugate sum verification. Zero-backaction categorical queries enable trans-Planckian temporal precision and  $\mathcal{O}(1)$  harmonic network access. Quadratic information scaling via reflectance cascade provides  $\mathcal{O}(N^3)$  total information from  $N$  observations. Hierarchical BMD networks maintain irreducible categorical completion history with compound states encoding inter-region interactions. Hardware stream phase-locked coupling grounds interpretation in measurable physical dynamics across multiple modalities. Categorical depth emerges from membrane thickness without geometric reconstruction. The modified HCCC algorithm implements S-distance minimization through dual-objective navigation balancing ambiguity maximization and stream coherence. Image understanding is navigation

through predetermined categorical manifolds constrained by hardware-stream measurements, providing finite categorical spaces accessible under real-time and energy budget constraints.

## References

- [1] David C Knill and Alexandre Pouget. The bayesian brain: the role of uncertainty in neural coding and computation. *Trends in Neurosciences*, 27(12):712–719, 2004.
- [2] Yann LeCun, Yoshua Bengio, and Geoffrey Hinton. Deep learning. *Nature*, 521(7553):436–444, 2015.
- [3] Kundai Farai Sachikonye Mataranyika. Categorical completion resolution of gibbs’ mixing paradox through oscillatory entropy. In preparation, 2025.
- [4] Kundai Farai Sachikonye Mataranyika. Consciousness as categorical completion: Solving the hard problem through oxygen-mediated oscillatory hole generation. In preparation, 2025.
- [5] Kundai Farai Sachikonye Mataranyika. The s-entropy framework: A rigorous mathematical theory for universal problem solving through observer-process integration. In preparation, 2025.
- [6] David Mumford. The bayesian rationale for energy functionals. In *Geometry-Driven Diffusion in Computer Vision*, pages 141–153. Springer, 1994.